Physics of Fluids

Unified gas-kinetic wave–particle method for gas–particle two-phase flow from dilute to dense solid particle limit

Cite as: Phys. Fluids **34**, 023312 (2022); https://doi.org/10.1063/5.0081105
Submitted: 06 December 2021 • Accepted: 21 January 2022 • Published Online: 08 February 2022

Xiaojian Yang, Wei Shyy and Kun Xu

Physics of Fluids ARTICLE scitation.org/journal/phf

Unified gas-kinetic wave–particle method for gas–particle two-phase flow from dilute to dense solid particle limit

Cite as: Phys. Fluids **34**, 023312 (2022); doi: 10.1063/5.0081105
Submitted: 6 December 2021 · Accepted: 21 January 2022 ·
Published Online: 8 February 2022

Xiaojian Yang,[1,a)] Wei Shyy,[1,a)] and Kun Xu[1,2,3,a)]

AFFILIATIONS

[1]Department of Mechanical and Aerospace Engineering, Hong Kong University of Science and Technology, Clear Water Bay, Kowloon, Hong Kong, China
[2]Department of Mathematics, Hong Kong University of Science and Technology, Clear Water Bay, Kowloon, Hong Kong, China
[3]Shenzhen Research Institute, Hong Kong University of Science and Technology, Shenzhen, China

[a)]**Authors to whom correspondence should be addressed:** xyangbm@connect.ust.hk; weishyy@ust.hk; makxu@ust.hk

ABSTRACT

A unified framework for particulate two-phase flow is presented with a wide range of solid particle concentration from dilute to dense limit. The two-phase flow is simulated by two coupled flow solvers, that is, the gas-kinetic scheme (GKS) for the gas phase and unified gas-kinetic wave–particle method (UGKWP) for the solid particle phase. The GKS is a second-order Navier–Stokes flow solver. The UGKWP is a multi-scale method for all flow regimes. The wave and particle decomposition in UGKWP depends on the cell's Knudsen number (Kn). At a small Kn number, the highly concentrated solid particle phase will be modeled by the Eulerian hydrodynamic wave due to the intensive particle–particle collisions. At a large Kn number, the dilute solid particle will be followed by the Lagrangian particle to capture the non-equilibrium transport. In the transition regime, a smooth transition between the above limits is obtained according to the local Kn number. The distribution of solid particles in UGKWP is composed of analytical function and discrete particle, and both condensed and dilute phases can be automatically captured in the most efficient way. In the current scheme, the two-phase model improves the previous one in many aspects, such as drag force model, the frictional pressure formulation, and flux limiting model. The scheme is tested in many typical gas–particle two-phase problems, including the interaction of shock wave with solid particle layer, horizontal pneumatic conveying, bubble formation, and particle cluster phenomena in the fluidized bed. The results validate the GKS-UGKWP for the simulation of gas–particle flow.

I. INTRODUCTION

Gas–particle two-phase flow is very common in nature, for example, sand storms, volcano eruption, and in many engineering industries, such as the petroleum industry, chemical industry, and energy industry. Numerical simulation is a powerful tool to study the gas– particle two-phase flow, and many numerical methods have been developed to accurately and efficiently capture the complex physics of gas–particle flow.[11,17,59,61,63,76]

In general, two approaches, the Eulerian–Eulerian (EE) approach and the Eulerian–Lagrangian (EL) approach, are widely employed, and the difference of this classification is based on the treatment of particle phase. In the EE approach, the particle phase is assumed as a continuum media, and hydrodynamic equations are employed for the evolution of particle flow.[22,47,49,50] EE approach is also called two-fluid model (TFM). One representative EE approach is kinetic theory-based granular flow (KTGF), which is based on the similarity in the modeling of solid particle and the molecule in gas.[15,34] In the EL approach, all individual solid particles or particle parcels are tracked according to Newton's law of motion in the simulation.[19,52] Some typical EL approaches are discrete element method (DEM),[12,19,60] coarse-grained particle method (CGPM),[35,48,74] multiphase particle-in-cell (MP-PIC),[1,40,41] etc. In terms of the consideration of flow physics, the choice of EE or EL depends on the local Knudsen (Kn) number of particle flow. Similar to gas, the Kn number of disperse phase can be defined as the ratio of mean free path (MFP) of solid particles over characteristic length scale.[37] When the Kn number is very small with sufficient inter-particle collisions, the solid particle phase can be assumed as a continuum medium, and the EE approach can be appropriately used for the gas–particle system. On the contrary, when the Kn number is large, individual particle transport becomes important and the solid

phase stays in a non-equilibrium state. As such, the EL approach is a preferred choice. The disadvantage of EL approach is the high computational cost due to the particle trajectory tracking for all individual particles or parcels, especially in the dense solid particle flow.[61] Theoretically, EL approach can be used when Kn number is small as long as the computation cost is affordable. For the EE approach, it will difficult to give an accurate prediction when Kn number of particle phase is large, because EE approach cannot capture non-equilibrium physics of solid particles, such as particle trajectory crossing (PTC) phenomenon.[2,37] Based on the features of EE and EL approach, many studies focus on the hybrid method, coupling Eulerian, and Lagrangian approach together for solid particle phase, to maintain both the accuracy and computation efficiency.[8,42,44,73] In the hybrid method, it is a challenge to define an accurate and reliable criterion for the smooth transition between the Eulerian and Lagrangian approaches for disperse phase. In addition, some other methods are proposed and used for the gas–particle flow, such as direct numerical simulation (DNS),[27,33] unified gas kinetic scheme (UGKS),[29,69] unified gas kinetic particle method (UGKP),[64] discrete unified gas kinetic scheme (DUGKS),[57] method of moment (MOM),[14,37] direct simulation Monte Carlo (DSMC),[4] material point method (MPM),[3] smooth particle hydrodynamics (SPH),[13] hybrid coarse-grain DEM and resolved DEM,[45] and hybrid finite-volume-particle method[10].

In recent years, unified gas-kinetic scheme (UGKS) has been developed for rarefied and continuum flow simulation.[67,69] Based on the direct modeling on the cell's Knudsen number, that is, $Kn_c = \tau/\Delta t$ with particle collision time τ over numerical time step Δt, UGKS recovers multiscale transport in flow regimes through a smooth connecting between $(1 - e^{-1/Kn_c})$ weighted equilibrium flow evolution and the rest e^{-1/Kn_c} particle free transport, and the NS solution is automatically obtained at small Kn_c. After the success of the UGKS for the gas flow, the method has been further extended to other multiscale transports, such as radiative heat transfer, neutron transport, plasma, and particulate flow.[29,30,55,56] A particle-based UGKS, which is named unified gas-kinetic particle (UGKP) method, was developed subsequently using stochastic particles to follow the evolution of gas distribution function.[32,77] In UGKP, the sampled particles can be divided into two categories: collisionless (free transport) particle and collisional particle within each time step. The collisional particles will be eliminated in the evolution and get re-sampled from the equilibrium state at the beginning of the next time step. As a result, only the collisionless particles are fully tracked in the whole time step in UGKP. Furthermore, it is realized that a proportion of $(1 - e^{-1/Kn_c})$ re-sampled particles from the equilibrium state at the beginning of next time step in UGKP will get collision and be eliminated again within the next time step. Actually, the contribution from these re-sampled collisional particles to flux function in the finite volume UGKP can be evaluated analytically. As a result, the collisional particles do not need to be re-sampled at all and can be followed analytically through a wave representation in the upgraded unified gas-kinetic wave–particle (UGKWP) method.[9,32,70,77] In UGKWP, wave and particle are coupled together in the evolution, and only free transport particles are basically tracked to capture the non-equilibrium flow physics. Therefore, UGKWP becomes a hydrodynamic flow solver in the continuum flow regime due to the absence of particles and goes to a particle method in the highly rarefied regime. UGKWP can present an optimized approach to capture multiscale transport efficiently using the combination of wave and particle. In the continuum flow regime, UGKWP will automatically get back to the gas-kinetic scheme (GKS), which is a kinetic theory-based Navier–Stokes solver.[7,24,65,66,71,75] In addition to gas flow, UGKWP has also been used in the study of radiative transfer, plasma, and two phase flow.[28,31,68,72] The special wave and particle decomposition in UGKWP make it suitable for the simulation of both dense (wave) and dilute solid particle (particle) phase easily.

For the particulate two-phase flow, the gas phase will be followed by the GKS and solid particle phase by the UGKWP, and final scheme is called GKS-UGKWP for convenience. For the dilute monodisperse particulate flow, a previous GKS-UGKWP has been developed.[72] Based on the UGKWP for the solid particle phase, the sampled particles depends on the local particle's cell's Knudsen number. When Kn_c is extremely small for dense particle distribution, no particle will be sampled in UGKWP and UGKWP reduces to the hydrodynamic flow solver. As a result, the GKS-UGKWP automatically becomes an EE approach. When Kn number is extremely large, only particle evolution in UGKWP will be tracked and the corresponding GKS-UGKWP becomes an EL approach. For the intermediate Kn_c number, both EE and EL formulation will be coupled in each cell according to Kn_c in the evolution of the particulate flow. In this paper, more realistic model will be implemented in GKS-UGKWP for the two-phase flow simulation.

Based on solid volume fraction ϵ_s, the particulate flow is usually divided into dilute flow with $\epsilon_s \leq \epsilon_s^*$ and dense flow $\epsilon_s > \epsilon_s^*$, and one of the choices of ϵ_s^* is 0.001.[62] However, the solid volume fraction is not necessarily a reliable parameter showing the importance of particle–particle collision, but the Knudsen number is a suitable indicator.[37] In general, the inter-particle collision is (much possibly but not necessarily) more frequent in dense flow than dilute one due to a large number of solid particles. Therefore, the particle–particle collision usually plays a significant role in the solid phase evolution of dense phase, and it cannot be neglected in the numerical simulation aiming to accurately recover the real flow physics. The influence of inter-particle collision is considered and modeled differently in numerical methods. For example, in MP-PIC, an inter-particle stress term models the effect of particle–particle collision, but it can only simulate the particulate flow with solid concentration $\epsilon_s < 0.05$, which cannot be very high.[1] With the modification of collision term, the improved MP-PIC can be used for dense particle flow with high concentration.[40,41] In DEM, both soft-sphere model and hard-sphere model can be used to calculate the influence of inter-particle collision.[12,21,59] In UGKWP, the collision effect is explicitly included in the collision term of the kinetic equation for modeling the evolution process from local non-equilibrium to equilibrium state.[32,36] For the numerical simulation of dense solid particle flow, a challenge is the existence of non-conservative "nozzle term" in momentum equation and correspondingly pDV work term in energy equation for the gas flow, which is similar to pDV term in the quasi-one-dimensional gas nozzle flow equation.[22] If these terms were not solved correctly, unphysical fluctuations of pressure and flow field would be generated, especially in the flow zone with a steep interface of solid-phase concentration.[22,49] When the solid-phase approaches to a packing limit, the effect of enduring particle–particle contact and friction, modeled by the solid frictional pressure term, has to be considered.[25,51,54] Also, the introduction of frictional pressure can avoid the solid particles'

over-assembling due to the dramatically increased value when the solid volume fraction approaches its maximum limiting value.[22,25] Particulate flow with high concentration is very common in practical engineering problems, such as fluidized bed and pneumatic conveying.[16,34,38] Therefore, in this paper, the previously developed GKS-UGKWP for dilute flow will be extended to dense gas–particle flow. The GKS-UGKWP is further developed for gas–particle two-phase flow with a wide range of volume fraction from very dilute flow to dense solid particle phase.

This paper is organized as follows. Section II introduces the governing equations for particle phase and the UGKWP method. Section III is the governing equations for gas phase and the GKS method. Section IV introduces the numerical experiments. Section V is the conclusion.

II. UGKWP FOR SOLID PARTICLE PHASE

A. Governing equation for particle phase

The evolution of particle phase is governed by the following kinetic equation:

$$\frac{\partial f_s}{\partial t}+\nabla_x\cdot(\mathbf{u}f_s)+\nabla_u\cdot(\mathbf{a}f_s)=\frac{g_s-f_s}{\tau_s}, \tag{1}$$

where $\mathbf{u}$ is the particle velocity, $\mathbf{a}$ is the particle acceleration caused by the external force, ∇_x is the divergence operator with respect to space, ∇_u is the divergence operator with respect to velocity, τ_s is the relaxation time for the particle phase, f_s is the distribution function of particle phase, and g_s is the associated equilibrium distribution, which can be written as

$$g_s=\epsilon_s\rho_s\left(\frac{\lambda_s}{\pi}\right)^{\frac{3}{2}}e^{-\lambda_s\left[(\mathbf{u}-\mathbf{U}_s)^2\right]},$$

where ϵ_s is the volume fraction of particle phase, ρ_s is the material density of particle phase, λ_s is the value relevant to the granular temperature T_s with $\lambda_s=\frac{m_s}{2k_BT_s}$, $m_s=\rho_s\frac{4}{3}\pi(\frac{d_s}{2})^3$ is the mass of one particle, d_s is the diameter of solid particle, and $\mathbf{U}_s$ is the macroscopic velocity of particle phase. The sum of kinetic and thermal energy for colliding particle may not be conserved due to the inelastic collision between particles. Therefore, the collision term in Eq. (1) should satisfy the following compatibility condition:[29]

$$\frac{1}{\tau_s}\int g_s\boldsymbol{\psi}\mathrm{d}\mathbf{u}=\frac{1}{\tau_s}\int f_s\boldsymbol{\psi}'\mathrm{d}\mathbf{u}, \tag{2}$$

where $\boldsymbol{\psi}=\left(1,\mathbf{u},\frac{1}{2}\mathbf{u}^2\right)^T$ and $\boldsymbol{\psi}'=\left(1,\mathbf{u},\frac{1}{2}\mathbf{u}^2+\frac{r^2-1}{2}(\mathbf{u}-\mathbf{U}_s)^2\right)^T$. The lost energy due to inelastic collision in 3D can be written as

$$Q_{loss}=\frac{(1-r^2)3p_s}{2},$$

where $r\in[0,1]$ is the restitution coefficient, determining the percentage of lost energy in inelastic collision. While $r=1$ means no energy loss (elastic collision), $r=0$ refers to total loss of all internal energy of particle phase $\epsilon_s\rho_se_s=\frac{3}{2}p_s$ with $p_s=\frac{\epsilon_s\rho_s}{2\lambda_s}$.

The particle acceleration $\mathbf{a}$ is determined by the external force. In this paper, the drag force $\mathbf{D}$, the buoyancy force $\mathbf{F}_b$, and gravity $\mathbf{G}$ are considered. $\mathbf{D}$ and $\mathbf{F}_b$ are inter-phase force, standing for the force applied on the solid particles by gas flow. The general form of drag force can be written as

$$\mathbf{D}=\frac{m_s}{\tau_{st}}(\mathbf{U}_g-\mathbf{u}), \tag{3}$$

where $\mathbf{U}_g$ is the macroscopic velocity of gas phase, and τ_{st} is the particle internal response time. Many studies have been conducted on the drag force model to give an accurate prediction for the drag under different solid concentrations. In this paper, the drag force model proposed by Gidaspow is employed to determine τ_{st}[18]

$$\tau_{st}=\begin{cases}\dfrac{4}{3}\dfrac{\rho_sd_s}{\rho_g|\mathbf{U}_g-\mathbf{u}|C_d}\epsilon_g^{2.65}, & \epsilon_g>0.8,\\ \dfrac{1}{150\dfrac{\epsilon_s\mu_g}{\epsilon_g\rho_sd_s^2}+1.75\dfrac{\rho_g|\mathbf{U}_g-\mathbf{u}|}{\rho_sd_s}}, & \epsilon_g\le 0.8\end{cases} \tag{4}$$

and it can used for both dilute and dense flow. C_d is the drag coefficient, which is obtained by

$$C_d=\begin{cases}\dfrac{24}{Re_s}\left(1+0.15Re_s^{0.687}\right), & Re_s\le 1000,\\ 0.44, & Re_s>1000,\end{cases} \tag{5}$$

where d_s is the diameter of solid particle, and μ_g is the dynamic viscosity of gas phase. $Re_s=|\mathbf{U}_g-\mathbf{u}|d_s/\nu_g$ is the particle Reynolds number, and $\nu_g=\mu_g/\rho_g$ is the kinematic viscosity of gas phase. In addition, another interactive force considered is the buoyancy force, which can be modeled as

$$\mathbf{F}_b=-\frac{m_s}{\rho_s}\nabla_xp_g, \tag{6}$$

where p_g is the pressure of gas phase. Then, the acceleration term can be obtained

$$\mathbf{a}=\frac{\mathbf{D}+\mathbf{F}_b}{m_s}+\mathbf{G}.$$

When the collision between solid particles is elastic with $r=1$, in the continuum flow regime the hydrodynamic equations becomes the Euler equations, which can be obtained based on the Chapman–Enskog asymptotic analysis

$$\begin{aligned}&\frac{\partial(\epsilon_s\rho_s)}{\partial t}+\nabla_x\cdot(\epsilon_s\rho_s\mathbf{U}_s)=0,\\ &\frac{\partial(\epsilon_s\rho_s\mathbf{U}_s)}{\partial t}+\nabla_x\cdot(\epsilon_s\rho_s\mathbf{U}_s\mathbf{U}_s+p_s\mathbb{I})\\ &\quad=\frac{\epsilon_s\rho_s(\mathbf{U}_g-\mathbf{U}_s)}{\tau_{st}}-\epsilon_s\nabla_xp_g+\epsilon_s\rho_s\mathbf{G},\\ &\frac{\partial(\epsilon_s\rho_sE_s)}{\partial t}+\nabla_x\cdot((\epsilon_s\rho_sE_s+p_s)\mathbf{U}_s)\\ &\quad=\frac{\epsilon_s\rho_s\mathbf{U}_s\cdot(\mathbf{U}_g-\mathbf{U}_s)}{\tau_{st}}-\frac{3p_s}{\tau_{st}}-\epsilon_s\mathbf{U}_s\cdot\nabla_xp_g+\epsilon_s\rho_s\mathbf{U}_s\cdot\mathbf{G}.\end{aligned} \tag{7}$$

Note that the heat conduction between the particle and gas phase is neglected in this paper. In summary, the evolution of particle phase is governed by Eq. (1), and the hydrodynamic equation (7) is only the asymptotic solution in the continuum flow limit for the solid particle phase.

B. UGKWP method

In this subsection, the UGKWP for the evolution of solid particle phase is introduced. In general, the kinetic equation of particle phase Eq. (1) is split as

$$\mathcal{L}_{s1}: \frac{\partial f_s}{\partial t} + \nabla_x \cdot (\mathbf{u} f_s) = \frac{g_s - f_s}{\tau_s}, \tag{8}$$

$$\mathcal{L}_{s2}: \frac{\partial f_s}{\partial t} + \nabla_u \cdot (\mathbf{a} f_s) = 0, \tag{9}$$

and splitting operator is used to solve Eq. (1). First, we focus on $\mathcal{L}_{s1}$ part, the particle phase kinetic equation without external force

$$\frac{\partial f_s}{\partial t} + \nabla_x \cdot (\mathbf{u} f_s) = \frac{g_s - f_s}{\tau_s}.$$

For brevity, the subscript s standing for the solid particle phase will be neglected in this subsection. The integration solution of the kinetic equation can be written as

$$f(\mathbf{x}, t, \mathbf{u}) = \frac{1}{\tau}\int_0^t g(\mathbf{x}', t', \mathbf{u}) e^{-(t-t')/\tau} \mathrm{d}t' + e^{-t/\tau} f_0(\mathbf{x} - \mathbf{u}t, \mathbf{u}), \tag{10}$$

where $\mathbf{x}' = \mathbf{x} + \mathbf{u}(t' - t)$ is the trajectory of particles, f_0 is the initial gas distribution function at time $t = 0$, and g is the corresponding equilibrium state.

In UGKWP, both macroscopic conservative variables and microscopic gas distribution function need to be updated. In general, in the finite volume framework, the cell-averaged macroscopic variables $\mathbf{W}_i$ of cell i can be updated by the conservation law

$$\mathbf{W}_i^{n+1} = \mathbf{W}_i^n - \frac{1}{\Omega_i}\sum_{S_{ij} \in \partial\Omega_i} \mathbf{F}_{ij} S_{ij} + \Delta t \mathbf{S}_i, \tag{11}$$

where $\mathbf{W}_i = (\rho_i, \rho_i \mathbf{U}_i, \rho_i E_i)$ is the cell-averaged macroscopic variables

$$\mathbf{W}_i = \frac{1}{\Omega_i}\int_{\Omega_i} \mathbf{W}(\mathbf{x}) \mathrm{d}\Omega.$$

Ω_i is the volume of cell i, $\partial\Omega_i$ denotes the set of cell interfaces of cell i, S_{ij} is the area of the jth interface of cell i, and $\mathbf{F}_{ij}$ denotes the macroscopic fluxes across the interface S_{ij}, which can be written as

$$\mathbf{F}_{ij} = \int_0^{\Delta t}\int \mathbf{u} \cdot \mathbf{n}_{ij} f_{ij}(\mathbf{x}, t, \mathbf{u}) \boldsymbol{\psi} \mathrm{d}\mathbf{u}\mathrm{d}t, \tag{12}$$

where $\mathbf{n}_{ij}$ is the normal unit vector of interface S_{ij}, $f_{ij}(t)$ is the time-dependent distribution function on the interface S_{ij}, and $\boldsymbol{\psi} = \left(1, \mathbf{u}, \frac{1}{2}\mathbf{u}^2\right)^T$. $\mathbf{S}_i$ is the source term due to inelastic collision inside each control volume, where the solid particle's internal energy has not been taken into account in the above equation.

Substituting the time-dependent distribution function Eq. (10) into Eq. (12), the fluxes can be obtained

$$\begin{aligned}
\mathbf{F}_{ij} &= \int_0^{\Delta t}\int \mathbf{u} \cdot \mathbf{n}_{ij} f_{ij}(\mathbf{x}, t, \mathbf{u}) \boldsymbol{\psi} \mathrm{d}\mathbf{u}\mathrm{d}t \\
&= \int_0^{\Delta t}\int \mathbf{u} \cdot \mathbf{n}_{ij} \left[\frac{1}{\tau}\int_0^t g(\mathbf{x}', t', \mathbf{u}) e^{-(t-t')/\tau} \mathrm{d}t'\right] \boldsymbol{\psi} \mathrm{d}\mathbf{u}\mathrm{d}t \\
&\quad + \int_0^{\Delta t}\int \mathbf{u} \cdot \mathbf{n}_{ij} \left[e^{-t/\tau} f_0(\mathbf{x} - \mathbf{u}t, \mathbf{u})\right] \boldsymbol{\psi} \mathrm{d}\mathbf{u}\mathrm{d}t \\
&\overset{def}{=} \mathbf{F}_{ij}^{eq} + \mathbf{F}_{ij}^{fr}.
\end{aligned}$$

The procedure of obtaining the local equilibrium state g_0 at the cell interface as well as the construction of $g(t)$ is the same as that in GKS. For a second-order accuracy, the equilibrium state g around the cell interface is written as

$$g(\mathbf{x}', t', \mathbf{u}) = g_0(\mathbf{x}, \mathbf{u})(1 + \bar{\mathbf{a}} \cdot \mathbf{u}(t' - t) + \bar{A}t'),$$

where $\bar{\mathbf{a}} = [\overline{a_1}, \overline{a_2}, \overline{a_3}]^T$, $\overline{a_i} = \frac{\partial g}{\partial x_i}/g$, $i = 1, 2, 3$, $\bar{A} = \frac{\partial g}{\partial t}/g$, and g_0 is the local equilibrium on the interface. Specifically, the coefficients of spatial derivatives $\overline{a_i}$ can be obtained from the corresponding derivatives of the macroscopic variables

$$\langle \overline{a_i} \rangle = \partial \mathbf{W}_0 / \partial x_i,$$

where $i = 1, 2, 3$, and $\langle \cdots \rangle$ means the moments of the Maxwellian distribution functions

$$\langle \cdots \rangle = \int \boldsymbol{\psi}(\cdots) g \mathrm{d}\mathbf{u}.$$

The coefficients of temporal derivative $\bar{A}$ can be determined by the compatibility condition

$$\langle \bar{\mathbf{a}} \cdot \mathbf{u} + \bar{A} \rangle = \begin{bmatrix} 0 \\ \mathbf{0} \\ -\dfrac{Q_{loss}}{\tau_s} \end{bmatrix}.$$

where $Q_{loss} = \frac{(1-r^2)3p_s}{2}$ is due to particle–particle inelastic collision. Now, all the coefficients in the equilibrium state $g(\mathbf{x}', t', \mathbf{u})$ have been determined, and its integration becomes

$$\begin{aligned}
f^{eq}(\mathbf{x}, t, \mathbf{u}) &\overset{def}{=} \frac{1}{\tau}\int_0^t g(\mathbf{x}', t', \mathbf{u}) e^{-(t-t')/\tau} \mathrm{d}t' \\
&= c_1 g_0(\mathbf{x}, \mathbf{u}) + c_2 \bar{\mathbf{a}} \cdot \mathbf{u} g_0(\mathbf{x}, \mathbf{u}) + c_3 A g_0(\mathbf{x}, \mathbf{u}),
\end{aligned} \tag{13}$$

with coefficients

$$\begin{aligned}
c_1 &= 1 - e^{-t/\tau}, \\
c_2 &= (t + \tau)e^{-t/\tau} - \tau, \\
c_3 &= t - \tau + \tau e^{-t/\tau}
\end{aligned}$$

and thereby, the integrated flux over a time step for equilibrium state can be obtained

$$\mathbf{F}_{ij}^{eq} = \int_0^{\Delta t}\int \mathbf{u} \cdot \mathbf{n}_{ij} f_{ij}^{eq}(\mathbf{x}, t, \mathbf{u}) \boldsymbol{\psi} \mathrm{d}\mathbf{u}\mathrm{d}t.$$

In addition, the flux contribution from the particle free transport f_0 is calculated by tracking the particles sampled from f_0. Therefore, the updating of the cell-averaged macroscopic variables can be written as

$$\mathbf{W}_i^{n+1} = \mathbf{W}_i^n - \frac{1}{\Omega_i}\sum_{S_{ij} \in \partial\Omega_i} \mathbf{F}_{ij}^{eq} S_{ij} + \frac{\mathbf{w}_i^{fr}}{\Omega_i} + \Delta t \mathbf{S}_i, \tag{14}$$

where $\mathbf{w}_i^{fr}$ is the net free streaming flow of cell i, standing for the flux contribution of the free streaming of particles, and the term $\mathbf{S}_i = [0, \mathbf{0}, -\frac{Q_{loss}}{\tau_s}]^T$ is the source term due to the inelastic collision for solid particle phase.

The net free streaming flow $\mathbf{w}_i^{fr}$ is determined in the following. The evolution of particle should also satisfy the integral solution of the kinetic equation, which can be written as

$$f(\mathbf{x},t,\mathbf{u}) = (1-e^{-t/\tau})g^{+}(\mathbf{x},t,\mathbf{u}) + e^{-t/\tau}f_0(\mathbf{x}-\mathbf{u}t,\mathbf{u}), \tag{15}$$

where g^{+} is named as the hydrodynamic distribution function with analytical formulation. The initial distribution function f_0 has a probability of $e^{-t/\tau}$ to free transport and $(1-e^{-t/\tau})$ to colliding with other particles. The post-collision particles satisfies the distribution $g^{+}(\mathbf{x},\mathbf{u},t)$. The free transport time before the first collision with other particles is denoted as t_c. The cumulative distribution function of t_c is

$$F(t_c < t) = 1 - e^{-t/\tau}, \tag{16}$$

and therefore, t_c can be sampled as $t_c = -\tau \ln(\eta)$, where η is a random number generated from a uniform distribution $U(0,1)$. Then, the free streaming time t_f for each particle is determined separately by

$$t_f = min\left[-\tau \ln(\eta), \Delta t\right], \tag{17}$$

where Δt is the time step. Therefore, within one time step, all particles can be divided into two groups: the collisionless particle and the collisional particle, and they are determined by the relation between of time step Δt and free streaming time t_f. Specifically, if $t_f = \Delta t$ for one particle, it is collisionless one, and the trajectory of this particle is fully tracked in the whole time step. On the contrary, if $t_f < \Delta t$ for one particle, it is collisional particle, and its trajectory will be tracked until t_f. The collisional particle is eliminated at t_f in the simulation, and the associated mass, momentum, and energy carried by this particle are merged into the macroscopic quantities in the relevant cell by counting its contribution through the flux function. More specifically, the particle trajectory in the free streaming process within time t_f is tracked by

$$\mathbf{x} = \mathbf{x}^n + \mathbf{u}^n t_f. \tag{18}$$

The term $\mathbf{w}_i^{fr}$ can be calculated by counting the particles passing through the interfaces of cell i

$$\mathbf{w}_i^{fr} = \sum_{k\in P(\partial\Omega_i^{+})} \phi_k - \sum_{k\in P(\partial\Omega_i^{-})} \phi_k, \tag{19}$$

where, $P(\partial\Omega_i^{+})$ is the particle set moving into the cell i during one time step, $P(\partial\Omega_i^{-})$ is the particle set moving out of the cell i during one time step, k is the particle index in one specific set, and $\phi_k = [m_k, m_k\mathbf{u}_k, \frac{1}{2}m_k(\mathbf{u}_k^2)]^T$ is the mass, momentum, and energy carried by particle k. Therefore, $\mathbf{w}_i^{fr}/\Omega_i$ is the net conservative quantities caused by the free stream of the tracked particles. Now, all the terms in Eq. (14) have been determined and the macroscopic variables $\mathbf{W}_i$ can be updated.

The trajectories of all particles have been tracked during the time interval $(0, t_f)$. For the collisionless particles with $t_f = \Delta t$, they still survive at the end of one time step; while the collisional particles with $t_f < \Delta t$ are deleted after their first collision, they are supposed to go to the equilibrium state in that cell. Therefore, the macroscopic variables of the collisional particles in cell i at the end of each time step can be directly obtained based on the conservation law

$$\mathbf{W}_i^h = \mathbf{W}_i^{n+1} - \mathbf{W}_i^p, \tag{20}$$

where $\mathbf{W}_i^{n+1}$ is the updated conservative variables in Eq. (14), and $\mathbf{W}_i^p$ are the mass, momentum, and energy of remaining collisionless particles in the cell at the end of the time step. In addition, the macroscopic variables $\mathbf{W}_i^h$ account for all eliminated collisional particles to the equilibrium state, and these particles can be re-sampling from $\mathbf{W}_i^h$ based on the overall Maxwellian distribution at the beginning of next time step. Now the updates of both macroscopic variables and the microscopic particles have been presented. The above method is the so-called unified gas-kinetic particle (UGKP) method.

The above UGKP can be further developed to UGKWP method. In UGKP method, all particles are divided into collisionless and collisional particles in each time step. The collisional particles are deleted after the first collision and re-sampled from $\mathbf{W}_i^h$ at the beginning of next time step. However, only the collisionless part of the re-samples particles can survive in the next time step, and all collisional ones will be deleted again. Actually, the transport fluxes from these collisional particles can be evaluated analytically without using particles. According to the cumulative distribution Eq. (16), the proportion of the collisionless particles is $e^{-\Delta t/\tau}$, and therefore, in UGKWP only the collisionless particles from the hydrodynamic variables $\mathbf{W}_i^h$ in cell i will be re-sampled with the total mass, momentum, and energy

$$\mathbf{W}_i^{hp} = e^{-\Delta t/\tau}\mathbf{W}_i^h. \tag{21}$$

Then, the free transport time of all the re-sampled particles will be $t_f = \Delta t$ in UGKWP. The fluxes $\mathbf{F}^{fr,wave}$ from these un-sampled collisional particle of $(1-e^{-\Delta t/\tau})\mathbf{W}_i^h$ can be evaluated analytically.[32,77] Now, same as UGKP, the net flux $\mathbf{w}_i^{fr,p}$ by the free streaming of the particles, which include remaining particles from previous time step and re-sampled collisionless ones, in UGKWP can be calculated by

$$\mathbf{w}_i^{fr,p} = \sum_{k\in P(\partial\Omega_i^{+})} \phi_k - \sum_{k\in P(\partial\Omega_i^{-})} \phi_k. \tag{22}$$

Then, the macroscopic flow variables in UGKWP are updated by

$$\mathbf{W}_i^{n+1} = \mathbf{W}_i^n - \frac{1}{\Omega_i}\sum_{S_{ij}\in\partial\Omega_i} \mathbf{F}_{ij}^{eq}S_{ij} - \frac{1}{\Omega_i}\sum_{S_{ij}\in\partial\Omega_i} \mathbf{F}_{ij}^{fr,wave}S_{ij} + \frac{\mathbf{w}_i^{fr,p}}{\Omega_i} + \Delta t\mathbf{S}_i, \tag{23}$$

where $\mathbf{F}_{ij}^{fr,wave}$ is the flux function from the un-sampled collisional particles.[32,68,77]

The second part $\mathcal{L}_{s2}$ in Eq. (9) accounts for the external acceleration

$$\frac{\partial f_s}{\partial t} + \nabla_u \cdot (\mathbf{a}f_s) = 0,$$

where the velocity-dependent acceleration term caused by inter-phase forces and solid particle's gravity has the following form:

$$\mathbf{a} = \frac{\mathbf{U}_g - \mathbf{u}}{\tau_{st}} - \frac{1}{\rho_s}\nabla_x p_g + \mathbf{G}.$$

Taking moment $\boldsymbol{\psi}$ to Eq. (9)

$$\int \boldsymbol{\psi}\left(\frac{\partial f_s}{\partial t} + \mathbf{a}\cdot\nabla_u f_s + f_s\nabla_u\cdot\mathbf{a}\right)\mathrm{d}\mathbf{u} = 0$$

and in the Euler regime with $f_s = g_s + \mathcal{O}(\tau_s)$, we can obtain

$$\frac{\partial \mathbf{W}_s}{\partial t} + \mathbf{Q}_s = 0,$$

where

$$\mathbf{W}_s = \begin{bmatrix} \epsilon_s \rho_s \\ \epsilon_s \rho_s \mathbf{U}_s \\ \epsilon_s \rho_s E_s \end{bmatrix},$$

$$\mathbf{Q}_s = \begin{bmatrix} 0 \\ \dfrac{\epsilon_s \rho_s (\mathbf{U}_s - \mathbf{U}_g)}{\tau_{st}} + \epsilon_s \nabla_x p_g - \epsilon_s \rho_s \mathbf{G} \\ \dfrac{\epsilon_s \rho_s \mathbf{U}_s \cdot (\mathbf{U}_s - \mathbf{U}_g)}{\tau_{st}} + 3\dfrac{p_s}{\tau_{st}} + \epsilon_s \mathbf{U}_s \cdot \nabla_x p_g - \epsilon_s \rho_s \mathbf{U}_s \cdot \mathbf{G} \end{bmatrix}.$$

When the first-order forward Euler method is employed for time marching, the cell-averaged macroscopic variable can be updated by

$$\mathbf{W}_s^{n+1} = \mathbf{W}_s - \mathbf{Q}_s \Delta t, \tag{24}$$

and the modifications on velocity and location of the remaining free transport particles can be written as

$$\mathbf{u}^{n+1} = \mathbf{u} + \mathbf{a} t_f, \tag{25}$$

$$\mathbf{x}^{n+1} = \mathbf{x} + \frac{\mathbf{a}}{2} t_f^2. \tag{26}$$

Now the update of the solid particle phase in one time step has been finished. In the following, specific variables determination for the solid particle phase will be presented.

C. Particle phase Knudsen number

The particle phase regime is determined by its Knudsen number Kn, defined by the ratio of collision time of solid particles τ_s to the characteristic time of macroscopic flow t_{ref},

$$Kn = \frac{\tau_s}{t_{ref}}. \tag{27}$$

Specifically, τ_s is the time interval between collisions of solid particles, or called the particle collision time, and t_{ref} is the characteristic time, defined as the ratio of flow characteristic length to the flow characteristic velocity, $t_{ref} = L_{ref}/U_{ref}$. According to the previous studies,[37,43] in this paper, τ_s is taken as

$$\tau_s = \frac{\sqrt{\pi} d_s}{12 \epsilon_s g_0} \sqrt{2\lambda_s}, \tag{28}$$

where d_s is the diameter of solid particle, ϵ_s is the volume fraction of solid phase, And g_0 is the radial distribution function with the following form:

$$g_0 = \frac{2 - c}{2(1 - c)^3}, \tag{29}$$

where $c = \epsilon_s / \epsilon_{s,max}$ is the ratio of the volume fraction ϵ_s to the allowed maximum value $\epsilon_{s,max}$. In general, for dilute particulate flow, τ_s is more likely much larger than t_{ref}, leading to a large Kn, and the particle transport plays more important role in the evolution. However, for dense particulate flow, the collision between solid particles is in high frequency, which results in a small τ_s and thereby a small Kn, and the inter-particle collision plays the key effect in the evolution.

D. Frictional pressure

When the solid phase is in high concentration, the frictional pressure p_{fric} has to be considered. p_{fric} accounts for the enduring inter-particle contacts and frictions, which play important roles in the near packing situation. Some expressions for p_{fric} have been proposed in the previous studies.[25,51,54] In this paper, the correlation proposed by Johnson and Jackson is employed,[22,25] which can be written as

$$p_{fric} = \begin{cases} 0, & \epsilon_s \le \epsilon_{s,crit}, \\ 0.1 \epsilon_s \dfrac{(\epsilon_s - \epsilon_{s,crit})^2}{(\epsilon_{s,max} - \epsilon_s)^5}, & \epsilon_s > \epsilon_{s,crit}, \end{cases} \tag{30}$$

where p_{fric} is with unit of Pa. $\epsilon_{s,crit}$ is the critical volume fraction of particle flow, and it takes a value 0.5 in this paper unless special notification. Therefore, the momentum and energy equation in Eq. (7) will be rewritten as

$$\frac{\partial (\epsilon_s \rho_s \mathbf{U}_s)}{\partial t} + \nabla_x \cdot \left(\epsilon_s \rho_s \mathbf{U}_s \mathbf{U}_s + p_s \mathbb{I} + p_{fric} \mathbb{I} \right) = \frac{\epsilon_s \rho_s (\mathbf{U}_g - \mathbf{U}_s)}{\tau_{st}} - \epsilon_s \nabla_x p_g + \epsilon_s \rho_s \mathbf{G}, \tag{31}$$

$$\frac{\partial (\epsilon_s \rho_s E_s)}{\partial t} + \nabla_x \cdot \left((\epsilon_s \rho_s E_s + p_s + p_{fric}) \mathbf{U}_s \right) = \frac{\epsilon_s \rho_s \mathbf{U}_s \cdot (\mathbf{U}_g - \mathbf{U}_s)}{\tau_{st}} - \frac{3 p_s}{\tau_{st}} - \epsilon_s \mathbf{U}_s \cdot \nabla_x p_g + \epsilon_s \rho_s \mathbf{U}_s \cdot \mathbf{G}. \tag{32}$$

The terms relevant to frictional pressure, $\nabla_x \cdot (p_{fric} \mathbb{I})$ and $\nabla_x \cdot (p_{fric} \mathbf{U}_s)$, are solved as source terms in this paper.

E. Flux limiting model near the packing condition

The introduction of frictional pressure p_{fric} can avoid the solid particles' over-assembling since it increases dramatically when the particle phase approaches its limiting packing state.[22,25] In addition, a flux limiting model is proposed in this paper to effectively prevent the solid volume fraction ϵ_s from exceeding its maximum value $\epsilon_{s,max}$. Taking one-dimensional example, in UGKWP the numerical flux at interface $i + 1/2$ between cell i and cell $i + 1$ can be generally written as

$$\mathbf{F}_{i+1/2} = \int_0^{\Delta t} \int_{u>0} u f_{i+1/2}(\mathbf{x}, t) \boldsymbol{\psi} \mathrm{d}u \mathrm{d}t + \int_0^{\Delta t} \int_{u<0} u f_{i+1/2}(\mathbf{x}, t) \boldsymbol{\psi} \mathrm{d}u \mathrm{d}t \overset{def}{=} \mathbf{F}^l_{i+1/2} + \mathbf{F}^r_{i+1/2}, \tag{33}$$

which will be modified as

$$\mathbf{F}_{i+1/2} = \mathbf{C}[\alpha(\epsilon_{s,i+1})] \cdot \mathbf{F}^l_{i+1/2} + \mathbf{C}[\alpha(\epsilon_{s,i})] \cdot \mathbf{F}^r_{i+1/2}, \tag{34}$$

with

$$\mathbf{C}[\alpha] = \begin{bmatrix} 1 - \alpha & 0 & 0 \\ 0 & 1 + \alpha & 0 \\ 0 & 0 & 1 - \alpha \end{bmatrix},$$

where α is the limiting factor, and it depends on the cell-averaged solid volume fraction ϵ_s as

$$\alpha(\epsilon_s) = \begin{cases} 0, & \epsilon_s \le k\epsilon_{s,max}, \\ \left(\dfrac{\epsilon_s - k\epsilon_{s,max}}{\epsilon_{s,max} - k\epsilon_{s,max}}\right)^2, & \epsilon_s > k\epsilon_{s,max}. \end{cases} \tag{35}$$

Here, k is a threshold for the flux limiting model, and it takes a value 0.95 unless special notification in this paper. As shown in Eq. (35), when ϵ_s is smaller than $k\epsilon_{s,max}$, the limiting factor α goes to 0 and there is no limiting; while when ϵ_s is larger than $k\epsilon_{s,max}$, α will increase and the limiting model works. Particularly, when the packing limit approaches to $\epsilon_s = \epsilon_{s,max}$, α also takes its maximum value 1. As a result, solid particles cannot flow into the "saturated" cell, and the solid volume fraction ϵ_s will not increase anymore. In addition, Eq. (34) indicates that, as this limiting model is activated, only the "inflow" across the interface will be effected, while the "outflow" will not be limited as a physical modeling to the reality.

III. GKS FOR GAS PHASE

A. Governing equation for gas phase

The gas phase is regarded as continuum flow, and the governing equations are the Navier–Stokes equations with source terms reflecting the inter-phase interaction[18,23]

$$\begin{aligned} &\frac{\partial(\widetilde{\rho}_g)}{\partial t} + \nabla_x \cdot (\widetilde{\rho}_g \mathbf{U}_g) = 0, \\ &\frac{\partial(\widetilde{\rho}_g \mathbf{U}_g)}{\partial t} + \nabla_x \cdot \left(\widetilde{\rho}_g \mathbf{U}_g \mathbf{U}_g + \widetilde{p}_g \mathbb{I}\right) - \epsilon_g \nabla_x \cdot (\mu_g \boldsymbol{\sigma}) \\ &\quad = p_g \nabla_x \epsilon_g - \frac{\epsilon_s \rho_s (\mathbf{U}_g - \mathbf{U}_s)}{\tau_{st}} + \widetilde{\rho}_g \mathbf{G}, \\ &\frac{\partial(\widetilde{\rho}_g E_g)}{\partial t} + \nabla_x \cdot \left(\left(\widetilde{\rho}_g E_g + \widetilde{p}_g\right)\mathbf{U}_g\right) \\ &\quad - \epsilon_g \nabla_x \cdot \left(\mu_g \boldsymbol{\sigma} \cdot \mathbf{U}_g - \kappa \nabla_x T_g\right) \\ &\quad = -p_g \frac{\partial \epsilon_g}{\partial t} - \frac{\epsilon_s \rho_s \mathbf{U}_s \cdot (\mathbf{U}_g - \mathbf{U}_s)}{\tau_{st}} + \frac{3p_s}{\tau_{st}} + \widetilde{\rho}_g \mathbf{U}_g \cdot \mathbf{G}, \end{aligned} \tag{36}$$

where $\widetilde{\rho}_g = \epsilon_g \rho_g$ is the apparent density of gas phase, $p_g = \rho_g R T_g$ is the pressure of gas phase and $\widetilde{p}_g = \widetilde{\rho}_g R T_g$, and the strain rate tensor $\boldsymbol{\sigma}$ is

$$\boldsymbol{\sigma} = \nabla_x \mathbf{U}_g + \left(\nabla_x \mathbf{U}_g\right)^T - \frac{2}{3} \nabla_x \cdot \mathbf{U}_g \mathbb{I},$$

and

$$\mu_g = \tau_g p_g, \quad \kappa = \frac{5}{2} R \tau_g p_g.$$

In particular, at the right-hand side in Eq. (36), the term $p_g \nabla_x \epsilon_g$ is called nozzle term, and the associated work term $-p_g \frac{\partial \epsilon_g}{\partial t}$ is called pDV work term, since it is similar to the pDV term in the quasi-one-dimensional gas nozzle flow equations.[22] Unphysical pressure fluctuations might occurs if the nozzle term and pDV term are not solved correctly. According to Ref. 58, Eq. (36) can be written as the following form:

$$\begin{aligned} &\frac{\partial(\rho_g)}{\partial t} + \nabla_x \cdot (\rho_g \mathbf{U}_g) = C_{\epsilon_g} \rho_g, \\ &\frac{\partial(\rho_g \mathbf{U}_g)}{\partial t} + \nabla_x \cdot \left(\rho_g \mathbf{U}_g \mathbf{U}_g + p_g \mathbb{I} - \mu_g \boldsymbol{\sigma}\right) \\ &\quad = C_{\epsilon_g} \rho_g \mathbf{U}_g - \frac{\epsilon_s \rho_s (\mathbf{U}_g - \mathbf{U}_s)}{\epsilon_g \tau_{st}} + \rho_g \mathbf{G}, \\ &\frac{\partial(\rho_g E_g)}{\partial t} + \nabla_x \cdot \left(\left(\rho_g E_g + p_g\right)\mathbf{U}_g - \mu_g \boldsymbol{\sigma} \cdot \mathbf{U}_g + \kappa \nabla_x T_g\right) \\ &\quad = C_{\epsilon_g} \left(\rho_g E_g + p_g\right) - \frac{\epsilon_s \rho_s \mathbf{U}_s \cdot (\mathbf{U}_g - \mathbf{U}_s)}{\epsilon_g \tau_{st}} + \frac{3p_s}{\epsilon_g \tau_{st}} + \rho_g \mathbf{U}_g \cdot \mathbf{G}, \end{aligned} \tag{37}$$

where $C_{\epsilon_g} = -\frac{1}{\epsilon_g}\frac{d\epsilon_g}{dt}$ with $\frac{d\epsilon_g}{dt} = \frac{\partial \epsilon_g}{\partial t} + \mathbf{U}_g \cdot \nabla \epsilon_g$, and how to solve C_{ϵ_g} in this paper will be introduced later.

B. GKS for gas evolution

This subsection introduces the evolution of gas phase in gas–particle two-phase system. The gas flow is governed by the Navier–Stokes equations with the inter-phase interaction, and the corresponding GKS is a limiting scheme of UGKWP in the continuum flow regime. In general, the evolution of gas phase Eq. (37) can be split into two parts

$$\mathcal{L}_{g1}: \begin{cases} \dfrac{\partial(\rho_g)}{\partial t} + \nabla_x \cdot (\rho_g \mathbf{U}_g) = 0, \\ \dfrac{\partial(\rho_g \mathbf{U}_g)}{\partial t} + \nabla_x \cdot \left(\rho_g \mathbf{U}_g \mathbf{U}_g + p_g \mathbb{I} - \mu_g \boldsymbol{\sigma}\right) = 0, \\ \dfrac{\partial(\rho_g E_g)}{\partial t} + \nabla_x \cdot \left(\left(\rho_g E_g + p_g\right)\mathbf{U}_g - \mu_g \boldsymbol{\sigma} \cdot \mathbf{U}_g + \kappa \nabla_x T_g\right) = 0, \end{cases} \tag{38}$$

$$\mathcal{L}_{g2}: \begin{cases} \dfrac{\partial(\rho_g)}{\partial t} = C_{\epsilon_g} \rho_g, \\ \dfrac{\partial(\rho_g \mathbf{U}_g)}{\partial t} = C_{\epsilon_g} \rho_g \mathbf{U}_g - \dfrac{\epsilon_s \rho_s (\mathbf{U}_g - \mathbf{U}_s)}{\epsilon_g \tau_{st}} + \rho_g \mathbf{G}, \\ \dfrac{\partial(\rho_g E_g)}{\partial t} = C_{\epsilon_g} \left(\rho_g E_g + p_g\right) - \dfrac{\epsilon_s \rho_s \mathbf{U}_s \cdot (\mathbf{U}_g - \mathbf{U}_s)}{\epsilon_g \tau_{st}} \\ \qquad\qquad + \dfrac{3p_s}{\epsilon_g \tau_{st}} + \rho_g \mathbf{U}_g \cdot \mathbf{G}. \end{cases} \tag{39}$$

The GKS is constructed to solve $\mathcal{L}_{g1}$ and $\mathcal{L}_{g2}$ separately. First, the kinetic equation without acceleration term for gas phase $\mathcal{L}_{g1}$ is

$$\frac{\partial f_g}{\partial t} + \nabla_x \cdot (\mathbf{u} f_g) = \frac{g_g - f_g}{\tau_g}, \tag{40}$$

where $\mathbf{u}$ is the velocity, τ_g is the relaxation time for gas phase, f_g is the distribution function of gas phase, and g_g is the corresponding equilibrium state (Maxwellian distribution). The local equilibrium state g_g can be written as

$$g_g = \rho_g \left(\frac{\lambda_g}{\pi}\right)^{\frac{K+3}{2}} e^{-\lambda_g\left[(\mathbf{u}-\mathbf{U}_g)^2 + \boldsymbol{\xi}^2\right]},$$

where ρ_g is the density of gas phase. λ_g is determined by gas temperature through $\lambda_g = \frac{m_g}{2k_B T_g}$, where m_g is the molecular mass, and $\mathbf{U}_g$ is the

macroscopic velocity of gas phase. K is the internal degree of freedom with $K = (5-3\gamma)/(\gamma-1)$ for three-dimensional diatomic gas, where $\gamma = 1.4$ is the specific heat ratio. The collision term satisfies the compatibility condition

$$\int \frac{g_g - f_g}{\tau_g}\boldsymbol{\psi}\mathrm{d}\Xi = 0, \tag{41}$$

where $\boldsymbol{\psi} = (1, \mathbf{u}, \frac{1}{2}(\mathbf{u}^2 + \boldsymbol{\xi}^2))^T$, the internal variables $\boldsymbol{\xi}^2 = \xi_1^2 + \cdots + \xi_K^2$, and $\mathrm{d}\Xi = \mathrm{d}\mathbf{u}\mathrm{d}\boldsymbol{\xi}$.

For Eq. (40), the integral solution of f at the cell interface can be written as

$$f(\mathbf{x}, t, \mathbf{u}, \boldsymbol{\xi}) = \frac{1}{\tau}\int_0^t g(\mathbf{x}', t', \mathbf{u}, \boldsymbol{\xi}) e^{-(t-t')/\tau}\mathrm{d}t' + e^{-t/\tau} f_0(\mathbf{x} - \mathbf{u}t, \mathbf{u}, \boldsymbol{\xi}), \tag{42}$$

where $\mathbf{x}' = \mathbf{x} + \mathbf{u}(t' - t)$ is the trajectory of particles, f_0 is the initial gas distribution function at time $t = 0$, and g is the corresponding equilibrium state. The initial NS gas distribution function f_0 in Eq. (42) can be constructed as

$$f_0 = f_0^l(\mathbf{x}, \mathbf{u})H(x) + f_0^r(\mathbf{x}, \mathbf{u})(1 - H(x)), \tag{43}$$

where $H(x)$ is the Heaviside function, f_0^l and f_0^r are the initial gas distribution functions on the left- and right-hand side of one cell interface. More specifically, the initial gas distribution function f_0^k, $k = l, r$, is constructed as

$$f_0^k = g^k\left(1 + \mathbf{a}^k \cdot \mathbf{x} - \tau(\mathbf{a}^k \cdot \mathbf{u} + A^k)\right),$$

where g^l and g^r are the Maxwellian distribution functions on the left- and right-hand sides of a cell interface, and they can be determined by the corresponding conservative variables $\mathbf{W}^l$ and $\mathbf{W}^r$. The coefficients, $\mathbf{a}^l = [a_1^l, a_2^l, a_3^l]^T$, $\mathbf{a}^r = [a_1^r, a_2^r, a_3^r]^T$, are related to the spatial derivatives in normal and tangential directions, which can be obtained from the corresponding derivatives of the initial macroscopic variables

$$\langle a_i^l \rangle = \partial \mathbf{W}^l / \partial x_i, \quad \langle a_i^r \rangle = \partial \mathbf{W}^r / \partial x_i,$$

where $i = 1, 2, 3$, and $\langle \cdots \rangle$ means the moments of the Maxwellian distribution functions

$$\langle \cdots \rangle = \int \boldsymbol{\psi}(\cdots) g \mathrm{d}\Xi.$$

Based on the Chapman–Enskog expansion, the non-equilibrium part of the distribution function satisfies

$$\langle \mathbf{a}^l \cdot \mathbf{u} + A^l \rangle = 0, \ \langle \mathbf{a}^r \cdot \mathbf{u} + A^r \rangle = 0,$$

and therefore, the coefficients A^l and A^r can be fully determined. The equilibrium state g around the cell interface is modeled as

$$g = g_0(1 + \bar{\mathbf{a}} \cdot \mathbf{x} + \bar{A}t), \tag{44}$$

where $\bar{\mathbf{a}} = [\bar{a}_1, \bar{a}_2, \bar{a}_3]^T$ and g_0 is the local equilibrium of the cell interface. More specifically, g can be determined by the compatibility condition

$$\int \boldsymbol{\psi} g_0 \mathrm{d}\Xi = \mathbf{W}_0 = \int_{u>0} \boldsymbol{\psi} g^l \mathrm{d}\Xi + \int_{u<0} \boldsymbol{\psi} g^r \mathrm{d}\Xi,$$
$$\int \boldsymbol{\psi}\bar{a}_i g_0 \mathrm{d}\Xi = \partial \mathbf{W}_0 / \partial x_i = \int_{u>0} \boldsymbol{\psi} a_i^l g^l \mathrm{d}\Xi + \int_{u<0} \boldsymbol{\psi} a_i^r g^r \mathrm{d}\Xi,$$

$i = 1, 2, 3$, and

$$\langle \bar{\mathbf{a}} \cdot \mathbf{u} + \bar{A} \rangle = 0.$$

After determining all parameters in the initial gas distribution function f_0 and the equilibrium state g, substituting Eqs. (43) and (44) into Eq. (42), the time-dependent distribution function $f(\mathbf{x}, t, \mathbf{u}, \boldsymbol{\xi})$ at a cell interface can be expressed as

$$\begin{aligned} f(\mathbf{x}, t, \mathbf{u}, \boldsymbol{\xi}) = {} & c_1 g_0 + c_2 \bar{\mathbf{a}} \cdot \mathbf{u} g_0 + c_3 \bar{A} g_0 \\ & + [c_4 g^r + c_5 \mathbf{a}^r \cdot \mathbf{u} g^r + c_6 A^r g^r](1 - H(u)) \\ & + [c_4 g^l + c_5 \mathbf{a}^l \cdot \mathbf{u} g^l + c_6 A^l g^l] H(u), \end{aligned} \tag{45}$$

with coefficients

$$\begin{aligned} c_1 &= 1 - e^{-t/\tau}, \\ c_2 &= (t + \tau)e^{-t/\tau} - \tau, \\ c_3 &= t - \tau + \tau e^{-t/\tau}, \\ c_4 &= e^{-t/\tau}, \\ c_5 &= -(t + \tau)e^{-t/\tau}, \\ c_6 &= -\tau e^{-t/\tau}. \end{aligned}$$

Then, the integrated flux over a time step can be obtained

$$\mathbf{F}_{ij} = \int_0^{\Delta t}\int \mathbf{u} \cdot \mathbf{n}_{ij} f_{ij}(\mathbf{x}, t, \mathbf{u}, \boldsymbol{\xi})\boldsymbol{\psi}\mathrm{d}\Xi\mathrm{d}t, \tag{46}$$

where $\mathbf{n}_{ij}$ is the normal vector of the cell interface. Then, the cell-averaged conservative variables of cell i can be updated as follows:

$$\mathbf{W}_i^{n+1} = \mathbf{W}_i^n - \frac{1}{\Omega_i}\sum_{S_{ij} \in \partial\Omega_i} \mathbf{F}_{ij} S_{ij}, \tag{47}$$

where Ω_i is the volume of cell i, $\partial\Omega_i$ denotes the set of interface of cell i, S_{ij} is the area of jth interface of cell i, $\mathbf{F}_{ij}$ denotes the projected macroscopic fluxes in the normal direction, and $\mathbf{W}_g = [\rho_g, \rho_g \mathbf{U}_g, \rho_g E_g]^T$ are the cell-averaged conservative flow variables for gas phase.

The second part, $\mathcal{L}_{g2}$, is from the inter-phase interaction. The increased macroscopic variables for gas phase in 3D can be calculated as

$$\mathbf{W}_g^{n+1} = \mathbf{W}_g + \mathbf{Q}\Delta t, \tag{48}$$

where

$$\mathbf{W}_g = \begin{bmatrix} \rho_g \\ \rho_g \mathbf{U}_g \\ \rho_g E_g \end{bmatrix},$$

$$\mathbf{Q} = \begin{bmatrix} C_{\epsilon_g}\rho_g \\ C_{\epsilon_g}\rho_g \mathbf{U}_g - \dfrac{\epsilon_s \rho_s (\mathbf{U}_g - \mathbf{U}_s)}{\epsilon_g \tau_{st}} + \rho_g \mathbf{G} \\ C_{\epsilon_g}(\rho_g E_g + p_g) - \dfrac{\epsilon_s \rho_s \mathbf{U}_s \cdot (\mathbf{U}_g - \mathbf{U}_s)}{\epsilon_g \tau_{st}} + \dfrac{3p_s}{\epsilon_g \tau_{st}} + \rho_g \mathbf{U}_g \cdot \mathbf{G} \end{bmatrix},$$

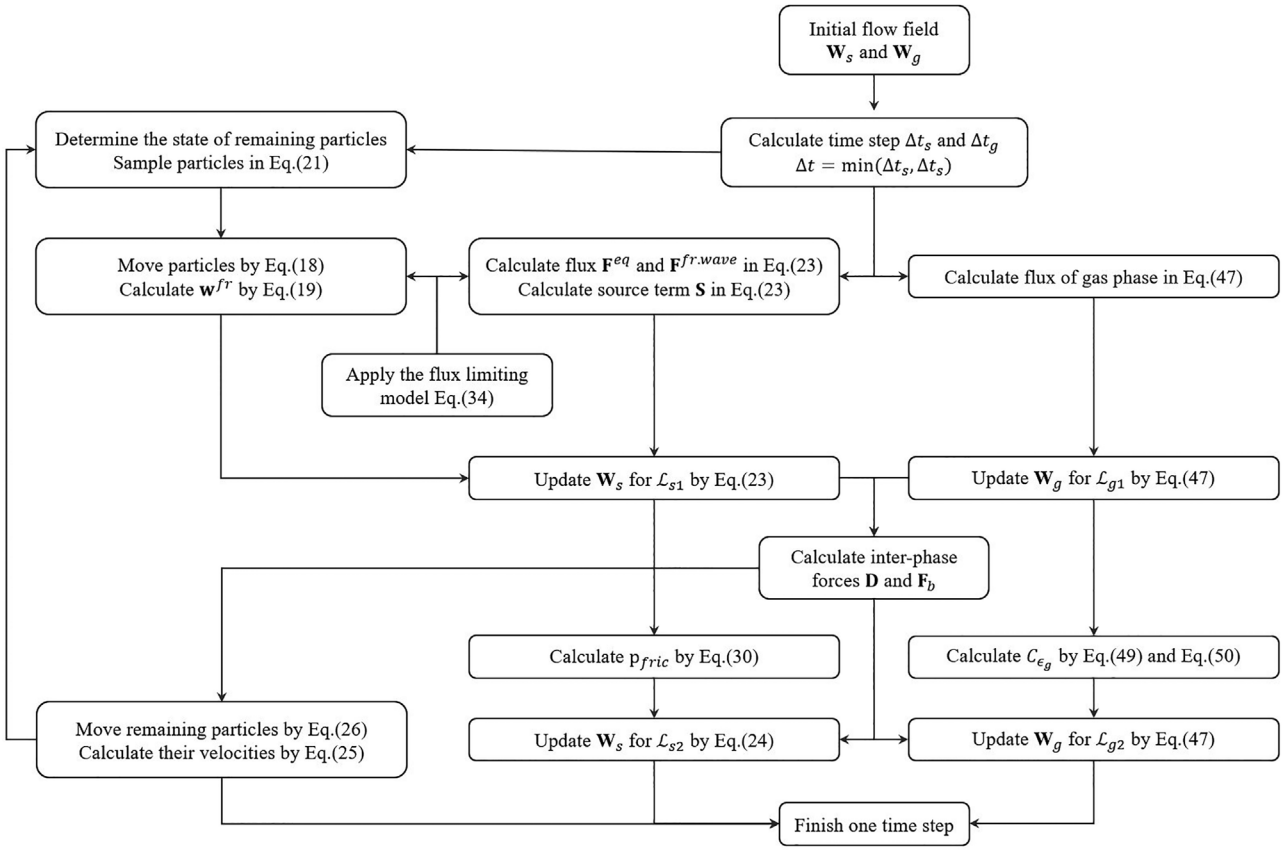

FIG. 1. The flow chart of GKS-UGKWP method.

with $C_{\epsilon_g} = -\frac{1}{\epsilon_g}\frac{\mathrm{d}\epsilon_g}{\mathrm{d}t}$ and $\frac{\mathrm{d}\epsilon_g}{\mathrm{d}t} = \frac{\partial \epsilon_g}{\partial t} + \mathbf{U}_g \cdot \nabla \epsilon_g$. In this paper, $\frac{\partial \epsilon_g}{\partial t}$ is evaluated

$$\frac{\partial \epsilon_g}{\partial t} = \frac{\epsilon_g^{n+1} - \epsilon_g^n}{\Delta t}. \tag{49}$$

Here, $\nabla \epsilon_g$ is the cell-averaged volume fraction gradient of gas phase in the cell. For example, $\frac{\partial \epsilon_g}{\partial x}$ is calculated by

$$\frac{\partial \epsilon_{g,i}}{\partial x} = \frac{\epsilon_{g,i+\frac{1}{2}} - \epsilon_{g,i-\frac{1}{2}}}{\Delta x}, \tag{50}$$

where $\epsilon_{g,i-\frac{1}{2}}$ and $\epsilon_{g,i+\frac{1}{2}}$ are volume fractions of gas phase at the left- and right-hand side of interface of cell i, which can be obtained from the reconstructed ϵ_s according to $\epsilon_s + \epsilon_g = 1$. Now the update for the gas phase in one time step has been finished.

Finally, the algorithm of GKS-UGKWP method for the gas–particle two-phase flow is summarized in Fig. 1.

IV. NUMERICAL EXPERIMENTS

A. Interaction of a shock wave with dense particle layer

The interaction of a shock wave with a dense particle layer will generate complicated particles' behavior,[26,53] which brings challenges to a numerical scheme. The problem in Ref. 26 is tested by GKS-UGKWP in this section. Figure 2 presents the initial configuration of the test case. The computational domain is a channel with size $L \times H = 0.1 \times 0.005\ \mathrm{m}^2$, which is covered by 250×20 uniform rectangular mesh. The initial height of the dense particle layer in the channel is 0.001 m, and the volume fraction is 0.5. The layer is composed of solid particles with density 1000 kg and diameter 90 μm. Initially, the gas in the channel is standard atmospheric condition. Next to the particle layer, there is a high pressure gas region with 4 bar, which will generate a shock wave after the diaphragm is removed at the beginning of calculation.

The post-shock snapshots of solid particle phase volume fraction are shown in Fig. 3. After the shock wave passes, more and more particles in the dense layer will be lifted upward and therefore a "particle

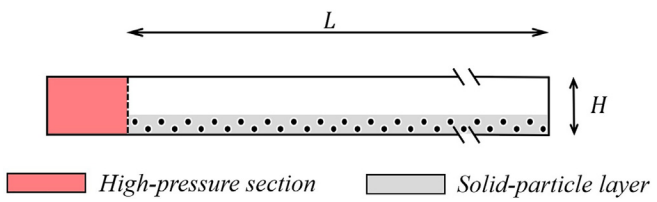

FIG. 2. Sketch of initial condition.

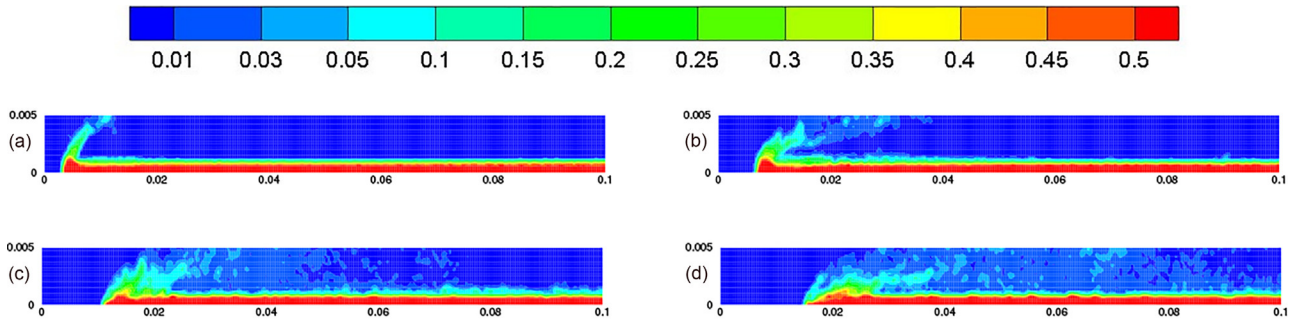

FIG. 3. Particle phase volume fraction at $t = 0.3$ ms, $t = 0.6$ ms, $t = 1.0$ ms, and $t = 1.4$ ms.

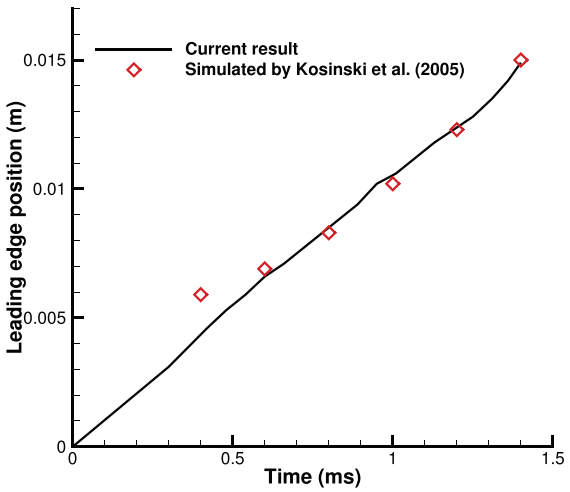

FIG. 4. The leading edge position of dense particle layer at different time.

stream" is formed at the leading section of the layer. The lifted particles will be accelerated by the gas flow, move forward, and are dispersed in the channel. These particle behaviors have also been observed in the previous studies.[26,53] Since more and more particles are lifted upward and dispersed in the channel, the leading edge of the dense particle layer gradually moves forward. The changing of leading-edge position with time is shown in Fig. 4, which agrees well with the previous study by Eulerian–Lagrangian approach.[26]

Figure 5 shows the wave and particle decompositions from UGKWP at $t = 1.0$ ms. For the dense particle layer region, for example, the zone near bottom wall, inter-particle collisions play the key role in the evolution due to the high solid concentration. In UGKWP, no particle will be sampled there and only wave is used for the evolution of particle flow, such as the automatic fluid approach. However, for the dilute particle region in the up part of the channel, the non-equilibrium particle transport appears and particles are sampled and tracked in UGKWP. Therefore, the UGKWP can adapt to different flow physics consistently. In addition, the percentage of sampled particles in UGKWP is fully determined by local flow condition, which is not artificially pre-defined. The above results indicate that UGKWP unifies the approaches for the equilibrium and non-equilibrium transport seamlessly and provides an efficient method for the multiscale flow simulation.

B. Horizontal pneumatic conveying

Pneumatic conveying is a widely used technique for the transportation of bulk solid particles by gas flow in the pipe or channel. The advantage of pneumatic conveying includes design flexibility, working safety, and low maintenance cost.[16] Under different conditions, the solid phase will show different flow patterns. Here, a horizontal pneumatic conveying problem will be tested by GKS-UGKWP to check its ability to recover the typical flow patterns. The flow conditions, including inlet gas velocity $U_{g,in}$, inlet solid mass flow rate $G_{s,in}$, and gas pressure gradient $\Delta p/L$, obtained from the experiment,[46] are employed in the simulation. The solid particles used in the experiment have the following physical properties: density $1683\,\mathrm{kg/m^3}$ and diameter 3.01 mm. The computational domain is a two-dimensional horizontal channel with size $4 \times 0.04\,\mathrm{m^2}$, covered by 800×8 uniform rectangular mesh. Three typical cases, disperse flow pattern, settle flow pattern, and slug flow pattern, are tested, and the corresponding experimental measurement data are listed in Table I. Initially, the gas with inlet velocity $U_{g,in}$ flows into the channel from the left boundary; the solid

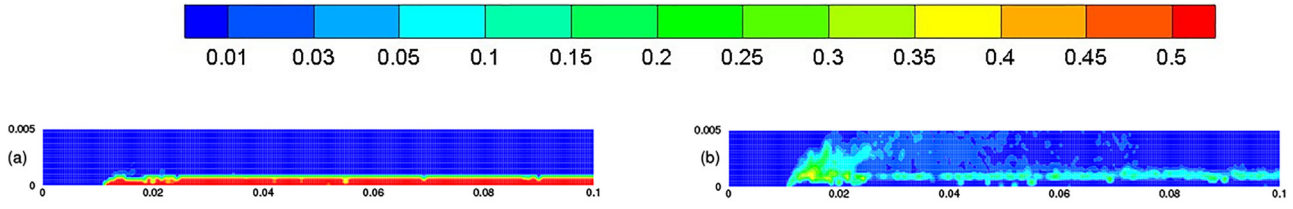

FIG. 5. UGKWP computation of solid particle phase by wave (a) and particle (b) decompositions at $t = 1.0$ ms.

TABLE I. Simulation conditions from experimental measurement.[46]

	$U_{g,in}$ (m/s)	$G_{s,in}$ (kg/m^2 s)	$\Delta p/L$ (Pa/m)	Flow pattern
Case 1	28.6	71.4	271.4	Disperse flow
Case 2	15.6	17.2	454.0	Settle flow
Case 3	10.4	21.1	855.6	Slug flow

particles are carried by gas flow and uniformly fed into the channel with mass flow rate $G_{s,in}$ through the left boundary; at the right boundary, solid particles are free to leave. The atmospheric pressure at right boundary is employed for gas phase, while higher gas pressure is imposed at the left boundary according to the pressure gradient $\Delta p/L$ given in Table I.

For case 1, the snapshot of solid phase volume fraction ϵ_s in the region 0.5–3.5 m at $t = 6.0$ s is shown in Fig. 6, and the enlarged snapshots at different times are presented in Fig. 7. The typical disperse flow pattern is observed: solid particles are dispersed in the whole channel with a low concentration and move downstream carried by gas flow; the solid concentration is relatively higher at the channel bottom than the up zone due to the effect of gravity. For case 2, the snapshot of solid volume fraction ϵ_s in the channel at $t = 6.0$ s and the enlarged snapshots in the local region 2.4–3.0 m are shown in Figs. 8 and 9, respectively. In case 2, a settled layer of solid particles with ϵ_s around 0.3 are formed along the channel bottom; while above this settle layer, the particle cloud is much more dilute than the settle layer, and particles are mainly transported in this zone. It is the typical structure for settle flow pattern, or called stratified flow pattern. Finally, the snapshot of solid volume fraction ϵ_s in the channel at 6.0 s for case 3 and the local enlarged snapshots at 5.0, 5.5, and 6.0 s are presented in Figs. 10 and 11. Compared with the flow conditions of case 2, case 3 has a lower inlet gas velocity and a greater inlet solid particle flux, and therefore, the solid concentration is generally higher in the channel. In particular, particle slugs are observed and moved in the channel, resulting in a dense particular flow across the whole cross section of the channel in certain regions, and the maximum concentration at the particle slug is close to the packing limit, which are the typical phenomena for the slug flow pattern. In summary, for three typical flow patterns, the primary flow structures in the experimental observations are well captured by GKS-UGKWP, validating the feasibility and reliability of GKS-UGKWP for this kind of problems.

C. Bubble formation in fluidized bed

The fluidized bed is widely used in chemical industry to enhance chemical reactions, solids separation, heat transfer, etc. In this problem, the initial stage of bubble formation in a fluidized bed is simulated, and the detailed description of this experiment can refer to Ref. 39. The sketch of this problem is shown in Fig. 12. The computational domain $W \times H$ is 0.57×1.0 m^2, and 76×120 uniform rectangular mesh is used. An orifice with width 0.02 m exists at the bottom center. The height of particle bed H_p is 0.5 m, and above this particle, bed is free board used for the expansion of particle bed. The bed consists of solid particles with density 3060 kg/m^3 and diameter 285 μm. The initial solid volume fraction ϵ_s is set as 0.5, which is smaller than $\epsilon_{s,max}$ taken as 0.6 in this case. This is based on the condition that the initial particle bed has reached a minimum fluidization state before blowing upward gas flow into the particle bed. Initially, the jet with $U_{jet} = 10.0$ m/s blows into the particle bed through the orifice, while the gas with the minimum fluidization velocity $U_{min} = 0.08$ m/s flows into the particle bed at other bottom boundary region outside the center orifice. For gas phase, the up boundary is set as pressure outlet, and for the bottom boundary a higher pressure is employed with

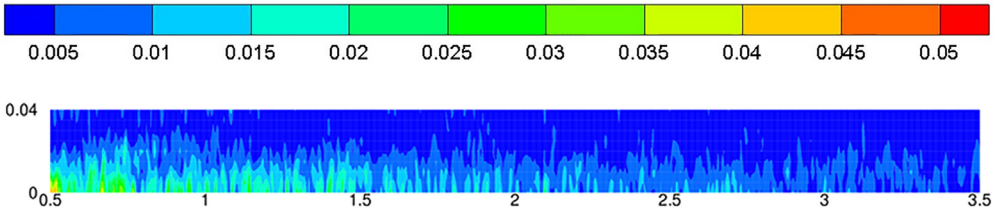

FIG. 6. The snapshot of solid phase volume fraction ϵ_s of case 1, disperse flow pattern, at $t = 6.0$ s.

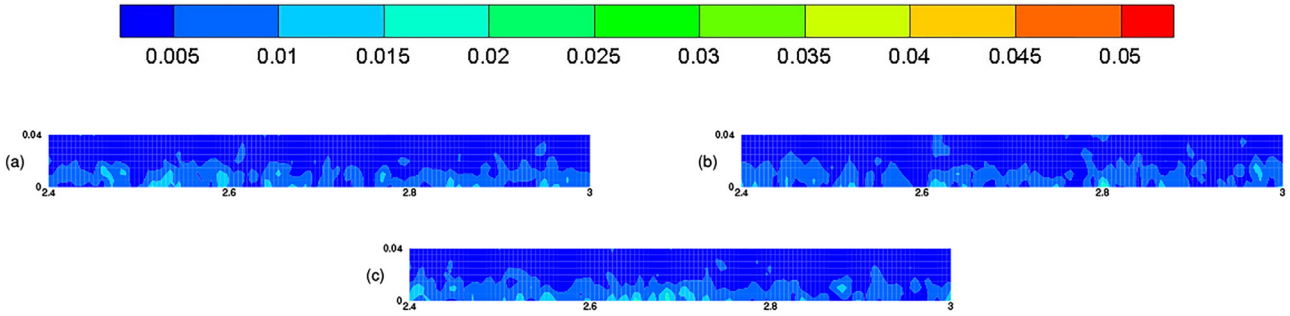

FIG. 7. The enlarged snapshots of solid phase volume fraction ϵ_s in the local region $2.4 - 3.0$ m of case 1 at different times: (a) $t = 5.0$ s, (b) $t = 5.5$ s, (c) $t = 6.0$ s.

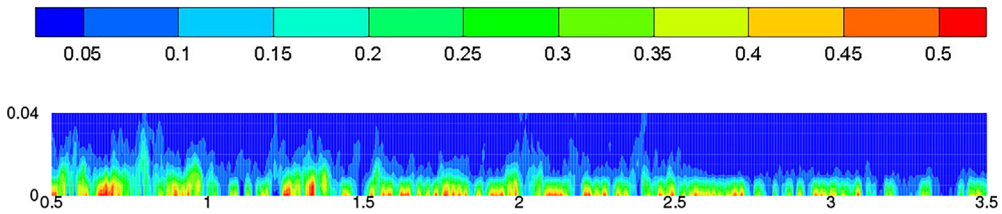

FIG. 8. The snapshot of solid phase volume fraction ϵ_s of case 2, settle flow pattern, at $t = 6.0$ s.

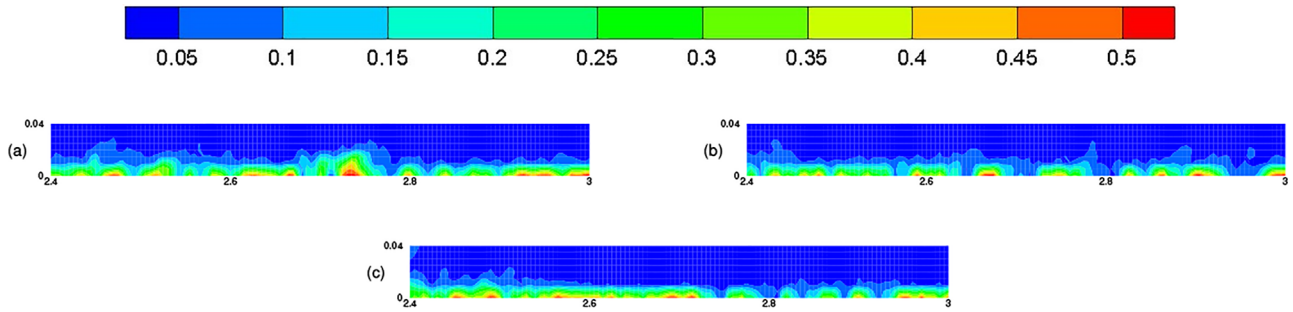

FIG. 9. The enlarged snapshots of solid phase volume fraction ϵ_s in the local region 2.4–3.0 m of case 2 at different times: (a) $t = 5.0$ s, (b) $t = 5.5$ s, (c) $t = 6.0$ s.

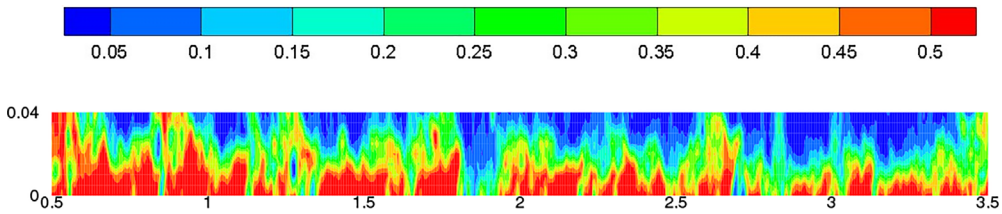

FIG. 10. The snapshot of solid phase volume fraction ϵ_s of case 3, slug flow pattern, at $t = 6.0$ s.

$\Delta p = 7500$ Pa, which is approximated to balance the gravity by $\Delta p = \epsilon_s(\rho_s - \rho_g)GH_p$ as given in Ref. 39. For the left and right walls, the non-slip and slip boundary condition is employed for gas phase and solid particle phase, respectively.

The contours of apparent density of solid particle phase at different times are shown in Fig. 13. The results show the typical process of bubble formation: initially, a small bubble occurs due to the jet with high velocity from the orifice; it becomes larger and larger in the evolution and finally detaches the bottom boundary. During the process, the bubble shape is similar to an ellipse. The above process obtained by GKS-UGKWP agrees well with the observed phenomenon in the experiment.[39] To further quantitatively compare the bubble formation process with the experiment, the equivalent bubble diameter is calculated, which is defined as $D_e = \sqrt{4S/\pi}$. According to Ref. 39, S is the area of bubble obtained by the numerical simulation, defined as the area of $\epsilon_s < 0.15$. The equivalent bubble diameter

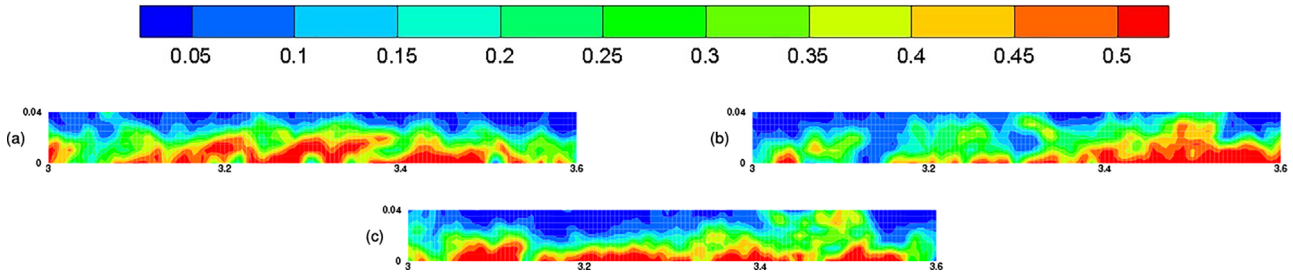

FIG. 11. The enlarged snapshots of solid phase volume fraction ϵ_s in the local region $3.0 - 3.6$ m of case 3 at different times: (a) $t = 5.0$ s, (b) $t = 5.5$ s, (c) $t = 6.0$ s.

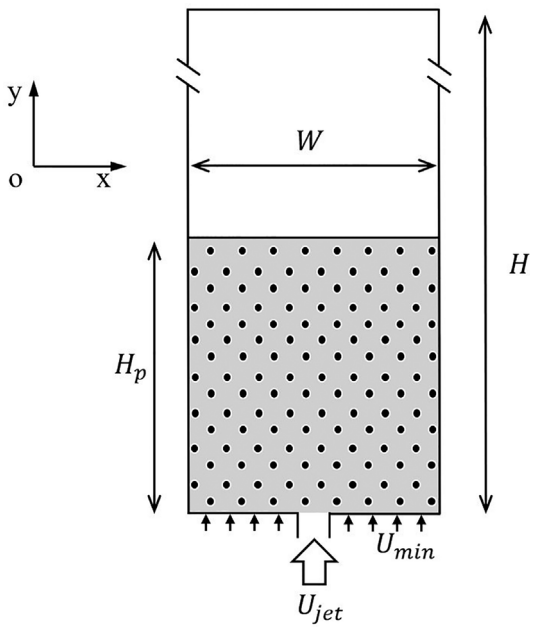

FIG. 12. Sketch of bubble formation in fluidized bed.

obtained by GKS-UGKWP is presented in Fig. 14, and it agrees well with the experiment measurement,[39] showing the accuracy and reliability of GKS-UGKWP. In order to clearly show the movement of solid particles in the bubble, the velocity field of the solid phase at $t = 0.18$ s is shown in Fig. 15. In the bottom zone of the bubble, solid particles from left and right sides move toward the center, and then move upward with a higher velocity carried by the gas flow. This particle behavior has also been found in the previous studies by both experiment and numerical simulation.[5] For this problem, the CPU time is about

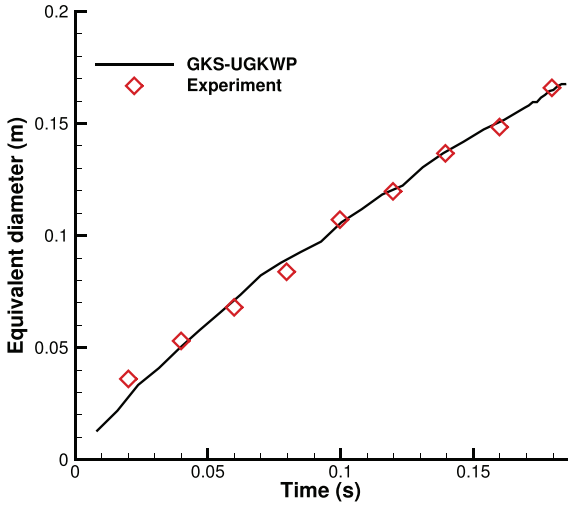

FIG. 14. Comparison of equivalent diameter D_e obtained by GKS-UGKWP with experiment measurement.

15 min by a single Intel core i7-9700 at 3.0 GHz. In addition, the sampled particles in UGKWP at different times are shown in Fig. 16. The original high-concentration solid particle bed is represented by wave and is not shown here. The sampled particles only appear in the non-equilibrium region, such as at the boundary between dense and dilute solid particle phase. In addition, as the gas bubble becomes larger, more particles will emerge in UGKWP to capture the larger non-equilibrium zone with the penetration of solid particles in the gas bubble region.

D. Particle clustering in fluidized bed

Particle clustering is a typical hydrodynamic phenomenon in circulating fluidized bed (CFB), and it has a significant influence on the

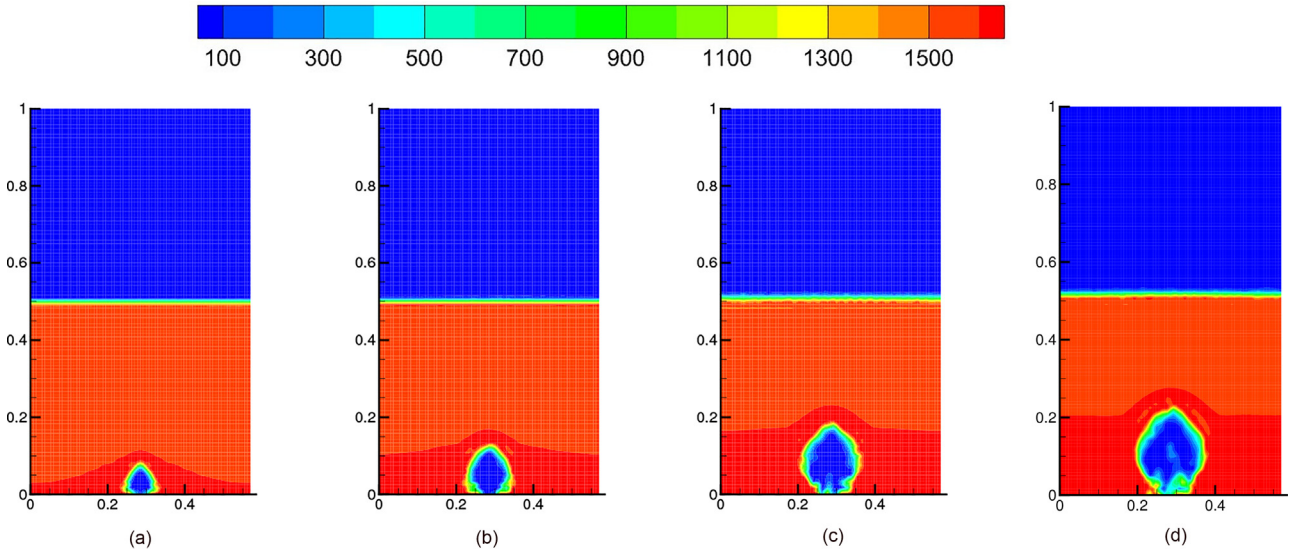

FIG. 13. Apparent density of solid particle phase during bubble formation process: from left to right are the snapshots at time 0.05, 0.10, 0.15, and 0.18 s.

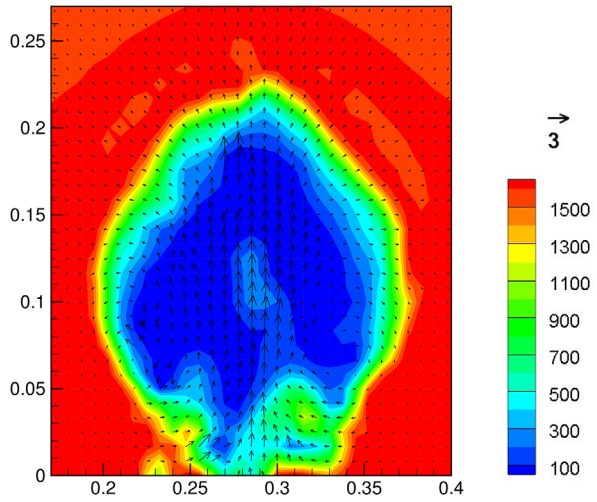

FIG. 15. The velocity field of the solid phase around the bubble at time 0.18 s, colored by the solid apparent density.

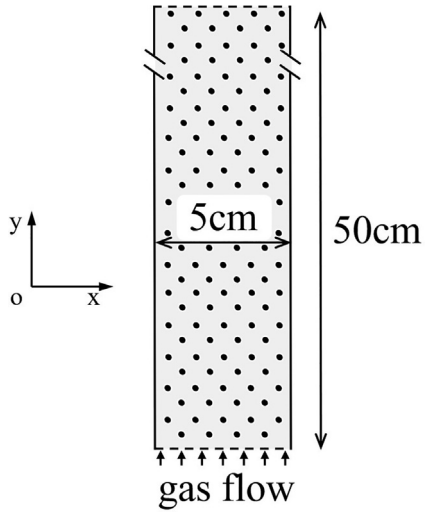

FIG. 17. Sketch of the vertical riser.

evolution of gas–particle flow.[6,20] In this section, GKS-UGKWP is used to calculate the CFB problem in Ref. 20 and capture the particle clustering phenomenon. Figure 17 presents the schematic diagram of the vertical riser in this problem. The computational domain $W \times H$ is $5 \times 50\,\mathrm{cm}^2$ covered by 25×250 uniform rectangular mesh. Initially, the solid particles are distributed uniformly in the riser with the solid phase volume fraction 0.03 and zero velocity; the gas phase is in standard atmospheric condition, $\rho_g = 1.2\,\mathrm{kg/m}^3$, $p = 1\,\mathrm{bar}$, and zero velocity. The density and diameter of the solid particles in the riser are $2400\,\mathrm{kg/m}^3$ and $133\,\mu\mathrm{m}$, respectively. Initially, the air flows into the riser through bottom boundary with vertical velocity $V_g = 1.0\,\mathrm{m/s}$ and higher pressure approximated by $\Delta p = \epsilon_s(\rho_s - \rho_g)GH$. The solid particles are free to leave at the up boundary, and the escaped particles from the up boundary will be compensated back into the riser through the bottom boundary to maintain the total mass of solid particles inside the riser in the whole simulation. For left and right walls, the slip and non-slip boundary conditions are employed for the solid phase and the gas phase, respectively.

The instantaneous snapshots of the distribution of solid volume fraction ϵ_s at different times are shown in Fig. 18. The results indicate that the typical heterogeneous structures in a circulating fluidized bed are captured clearly: axially, it is dilute flow in the upper zone while dense flow in the bottom zone; solid particles aggregate into clusters in the riser; generally, solid particles and clusters are carried upward in the core zone by high-speed gas flow while dropping down mainly at the near-wall zone. All the above typical features are consistent with the previous observations in both numerical and experimental studies.[20] In addition, the solutions from different mesh size with of 20×200 and 30×300 mesh points are compared. The instantaneous snapshots of solid volume fraction ϵ_s at time 5.0 s are shown in Fig. 19.

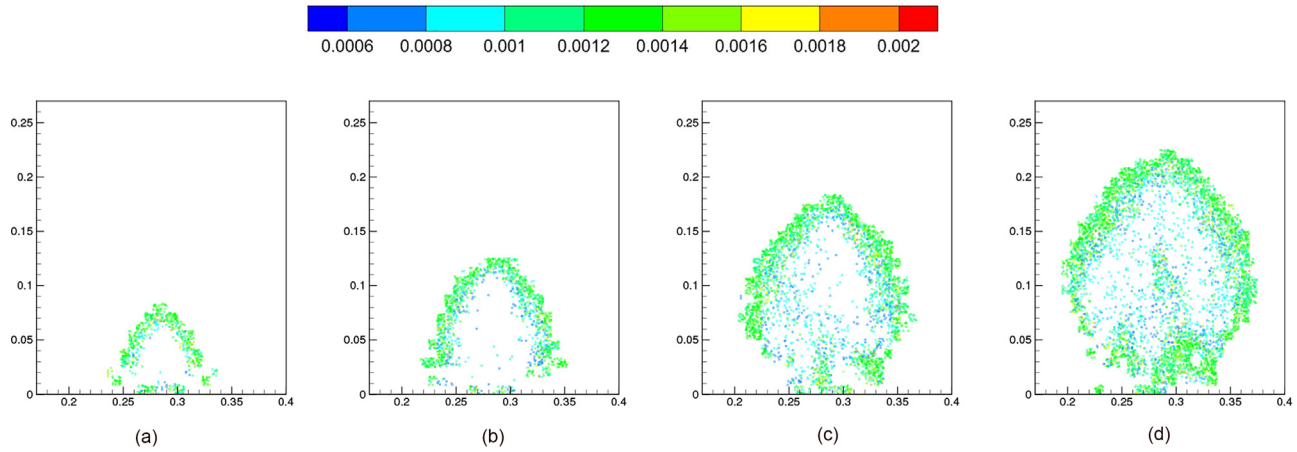

FIG. 16. Sampled particle for the solid particle phase in bubble formation process: from left to right are the results at time 0.05, 0.10, 0.15, and 0.18 s. The color shows the mass fraction of particle representation in UGKWP. The wave representation of solid particle phase in the dense particle zone is not shown here.

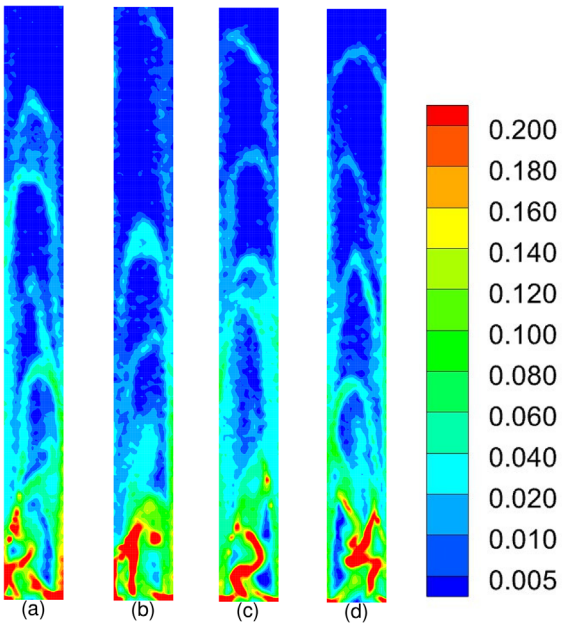

FIG. 18. The instantaneous snapshots of the distribution of solid phase volume fraction ϵ_s at different times: (a) $t = 3.0$ s, (b) $t = 4.0$ s, (c) $t = 5.0$ s, and (d) $t = 6.0$ s.

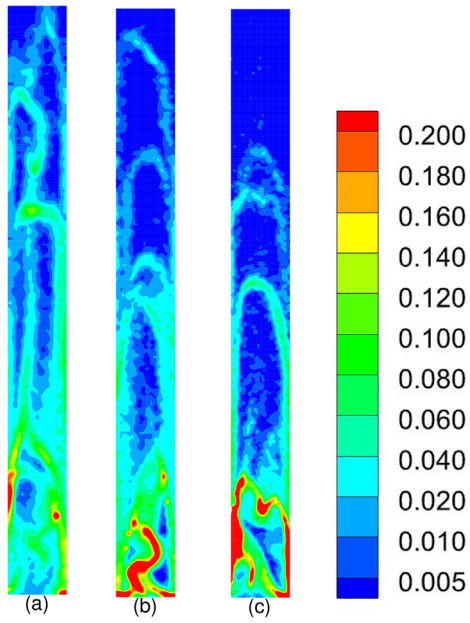

FIG. 19. The instantaneous snapshots of the distribution of solid phase volume fraction ϵ_s at $t = 5.0$ s, with different meshes: (a) 20×200, (b) 25×250, and (c) 30×300.

In general, two refined meshes give finer structures of the solid particle flow than the coarse mesh one. For example, the structure of clustered solid particles is more clear in Figs. 19(b) and 19(c), while solid particles are more dissipated in the whole riser in Fig. 19(a). Further, the profiles of time-averaged ϵ_s at different riser height for different mesh are shown in Fig. 20(a) and compared with the previous numerical results obtained by the Eulerian–Lagrangian approach.[20] In general, the results obtained by GKS-UGKWP under three meshes are similar with the previous study: the particle phase has a lower concentration about 0.01 in the upper zone, while a higher concentration 0.1 in the zone near bottom boundary. Also, further comparison shows the profiles of ϵ_s predicted by the refined mesh 25×250 and 30×300 agree

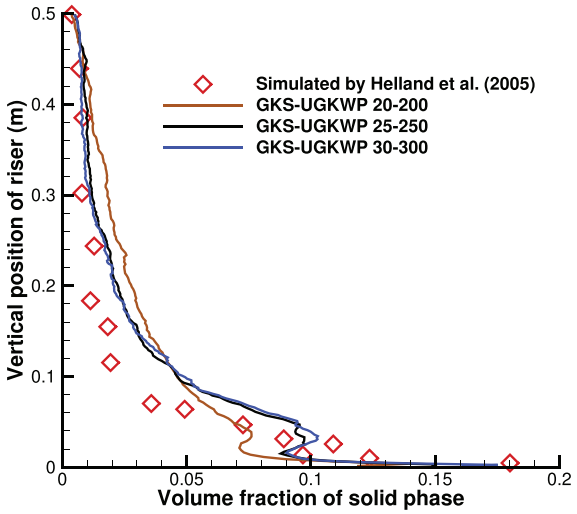

(a)

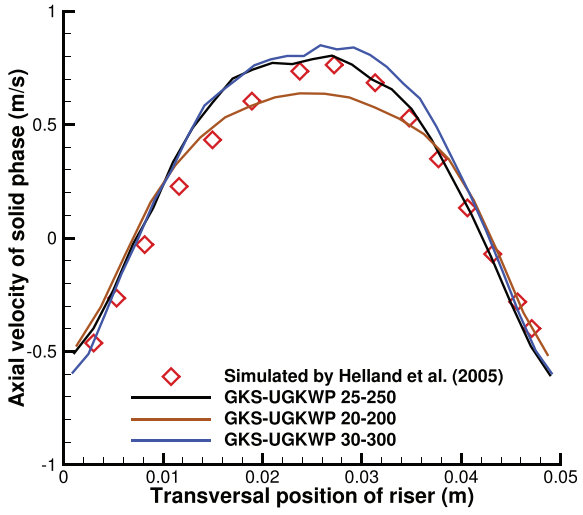

(b)

FIG. 20. Comparison with the numerical results by Eulerian–Lagrangian approach.[20] Left: time-averaged solid phase volume fraction ϵ_s at different height. Right: transversal profile of the time-averaged solid phase velocity vs in the upper part of the riser.

better than the coarse mesh one. Figure 20(b) presents the transversal profile of vertical velocity of particle flow, which shows a parabolic shape, indicating solid particles move upward in the center region, while downward in the near-wall zone. Overall, the prediction given by GKS-UGKWP agrees well with the previous study by Eulerian–Lagrangian approach.

V. CONCLUSION

In this paper, GKS-UGKWP method is developed to study gas–particle two-phase flow with both dense and dilute solid particle concentration. A drag force model for both dilute and dense particle flow is employed. The pressure model for inter-particle contacts and frictions is introduced, and it works for high solid particle concentration flow. In addition, a flux limiting model is proposed to prevent the over-packing of the solid particle phase. The non-conservative terms in the gas phase for accounting nozzle effect in momentum equation and *pDV* work term in the energy equation are added in the current scheme. For the particulate flow at high concentration, the inter-particle collisions play significant roles in the evolution. The inter-particle collision is included in the collision term of the kinetic equation for the particle phase to approach to the local equilibrium state. The current method can be used for particulate flow with a wide range of solid concentrations: from very dilute flow to dense one.

UGKWP is a multiscale method and is capable of capturing the multiscale transport of particulate flow efficiently by its coupled wave–particle formulation in the evolution process. At a small cell *Kn* number in high particle concentration region, the intensive inter-particle collisions will drive the particle distribution to near equilibrium and is represented by wave component in UGKWP without particles. As a result, the EE two-fluid approach can be recovered by UGKWP, the so-called coupled hydrodynamic equations for two-phase flow. While at large *Kn* number for dilute particle concentration, the inadequate inter-particle collision in UGKWP keeps the particle phase in non-equilibrium and its evolution is fully determined by the particle transport. The EL approach for the two-phase flow is obtained by UGKWP automatically in the dilute particle concentration region. At an intermediate *Kn* number, both wave and particle in UGKWP play roles in the evolution, and the number of sampled particles is determined by local Knudsen number for accounting the degree of non-equilibrium, which ensures a smooth and consistent transition in different flow regimes.

The proposed GKS-UGKWP for the gas–particle system is tested by a series of two-phase problems. The interaction of shock wave with solid particle layer in a channel is simulated, and the numerical results agree well with the previous study by EL approach. In the horizontal pneumatic conveying problem, typical flow patterns observed in the experiment for both low and high solid concentrations are well captured by GKS-UGKWP. The bubble formation through a particle bed is well captured by the proposed method, and the bubble shape and size agree well with the experiment measurements. Also in the circulating fluidized bed case, the particle clustering phenomenon and the corresponding heterogeneous structures are well captured by GKS-UGKWP. These results validate the accuracy and reliability of GKS-UGKWP for the simulation of gas–particle two-phase flow.

ACKNOWLEDGMENTS

The current research is supported by National Numerical Windtunnel project, National Science Foundation of China (No. 12172316), Hong Kong research Grant Council No. 16208021, and Department of Science and Technology of Guangdong Province (Grant No. 2020B1212030001).

AUTHOR DECLARATIONS

Conflict of Interest

The authors have no conflicts of interest to disclose.

DATA AVAILABILITY

The data that support the findings of this study are available from the corresponding authors upon reasonable request.

REFERENCES

[1]M. J. Andrews and P. J. O'Rourke, "The multiphase particle-in-cell (MP-PIC) method for dense particulate flows," Int. J. Multiphase Flow **22**(2), 379–402 (1996).
[2]S. Balachandar and J. K. Eaton, "Turbulent dispersed multiphase flow," Annu. Rev. Fluid Mech. **42**, 111–133 (2010).
[3]A. S. Baumgarten and K. Kamrin, "A general fluid-sediment mixture model and constitutive theory validated in many flow regimes," J. Fluid Mech. **861**, 721–764 (2019).
[4]G. A. Bird, "Molecular gas dynamics," NASA STI/Recon Technical Report A No. **76**:40225, 1976.
[5]G. A. Bokkers, M. van Sint Annaland, and J. A. M. Kuipers, "Mixing and segregation in a bidisperse gas–solid fluidised bed: A numerical and experimental study," Powder Technol. **140**(3), 176–186 (2004).
[6]S. A. Boronin and A. N. Osiptsov, "Effect of settling particles on the stability of a particle-laden flow in a vertical plane channel," Phys. Fluids **30**(3), 034102 (2018).
[7]G. Cao, H. Su, J. Xu, and K. Xu, "Implicit high-order gas kinetic scheme for turbulence simulation," Aerosp. Sci. Technol. **92**, 958–971 (2019).
[8]X. Chen and J. Wang, "Dynamic multiscale method for gas-solid flow via spatiotemporal coupling of two-fluid model and discrete particle model," AIChE J. **63**(9), 3681–3691 (2017).
[9]Y. Chen, Y. Zhu, and K. Xu, "A three-dimensional unified gas-kinetic wave-particle solver for flow computation in all regimes," Phys. Fluids **32**(9), 096108 (2020).
[10]A. Chertock, S. Cui, and A. Kurganov, "Hybrid finite-volume-particle method for dusty gas flows," SMAI J. Comput. Math. **3**, 139–180 (2017).
[11]A. K. Chinnappan, R. Kumar, and V. K. Arghode, "Modeling of dusty gas flows due to plume impingement on a lunar surface," Phys. Fluids **33**(5), 053307 (2021).
[12]P. A. Cundall and O. D. Strack, "A discrete numerical model for granular assemblies," Geotechnique **29**(1), 47–65 (1979).
[13]L. Deng, Y. Liu, W. Wang, W. Ge, and J. Li, "A two-fluid smoothed particle hydrodynamics (TF-SPH) method for gas-solid fluidization," Chem. Eng. Sci. **99**, 89–101 (2013).
[14]O. Desjardins, R. O. Fox, and P. Villedieu, "A quadrature-based moment method for dilute fluid-particle flows," J. Comput. Phys. **227**(4), 2514–2539 (2008).
[15]J. Ding and D. Gidaspow, "A bubbling fluidization model using kinetic theory of granular flow," AIChE J. **36**(4), 523–538 (1990).
[16]L.-S. Fan and C. Zhu, *Principles of Gas-Solid Flows* (Cambridge University Press, 1999).
[17]W. Ge, L. Wang, J. Xu, F. Chen, G. Zhou, L. Lu, Q. Chang, and J. Li, "Discrete simulation of granular and particle-fluid flows: From fundamental study to engineering application," Rev. Chem. Eng. **33**(6), 551–623 (2017).
[18]D. Gidaspow, *Multiphase Flow and Fluidization: Continuum and Kinetic Theory Descriptions* (Academic Press, 1994).
[19]Y. Guo and J. S. Curtis, "Discrete element method simulations for complex granular flows," Annu. Rev. Fluid Mech. **47**, 21–46 (2015).
[20]E. Helland, R. Occelli, and L. Tadrist, "Numerical study of cluster and particle rebound effects in a circulating fluidised bed," Chem. Eng. Sci. **60**(1), 27–40 (2005).
[21]B. P. B. Hoomans, J. A. M. Kuipers, W. J. Briels, and W. P. M. van Swaaij, "Discrete particle simulation of bubble and slug formation in a

two-dimensional gas-fluidised bed: A hard-sphere approach," Chem. Eng. Sci. **51**(1), 99–118 (1996).
[22]R. W. Houim and E. S. Oran, "A multiphase model for compressible granular-gaseous flows: Formulation and initial tests," J. Fluid Mech. **789**, 166 (2016).
[23]M. Ishii and T. Hibiki, *Thermo-Fluid Dynamics of Two-Phase Flow* (Springer Science and Business Media, 2006).
[24]X. Ji, F. Zhao, W. Shyy, and K. Xu, "A HWENO reconstruction based high-order compact gas-kinetic scheme on unstructured mesh," J. Comput. Phys. **410**, 109367 (2020).
[25]P. C. Johnson and R. Jackson, "Frictional-collisional constitutive relations for granular materials, with application to plane shearing," J. Fluid Mech. **176**, 67–93 (1987).
[26]P. Kosinski, A. C. Hoffmann, and R. Klemens, "Dust lifting behind shock waves: Comparison of two modelling techniques," Chem. Eng. Sci. **60**(19), 5219–5230 (2005).
[27]D. Li, A. Wei, K. Luo, and J. Fan, "Direct numerical simulation of a particle-laden flow in a flat plate boundary layer," Int. J. Multiphase Flow **79**, 124–143 (2016).
[28]W. Li, C. Liu, Y. Zhu, J. Zhang, and K. Xu, "Unified gas-kinetic wave-particle methods. III. Multiscale photon transport," J. Comput. Phys. **408**, 109280 (2020).
[29]C. Liu, Z. Wang, and K. Xu, "A unified gas-kinetic scheme for continuum and rarefied flows. VI. Dilute disperse gas-particle multiphase system," J. Comput. Phys. **386**, 264–295 (2019).
[30]C. Liu and K. Xu, "A unified gas kinetic scheme for continuum and rarefied flows. V. Multiscale and multi-component plasma transport," Commun. Comput. Phys. **22**(5), 1175–1223 (2017).
[31]C. Liu and K. XU, "Unified gas-kinetic wave-particle methods. IV. Multi-species gas mixture and plasma transport," Adv. Aerodyn. **3**(9), 9 (2021).
[32]C. Liu, Y. Zhu, and K. Xu, "Unified gas-kinetic wave-particle methods. I. Continuum and rarefied gas flow," J. Comput. Phys. **401**, 108977 (2020).
[33]X. Liu, L. Wang, and W. Ge, "Meso-scale statistical properties of gas–solid flow—A direct numerical simulation (DNS) study," AIChE J. **63**(1), 3–14 (2017).
[34]L. Huilin, D. Gidaspow, and S. Wang, *Computational Fluid Dynamics and the Theory of Fluidization: Applications of the Kinetic Theory of Granular Flow* (Springer Nature, 2021).
[35]L. Lu, J. Xu, W. Ge, G. Gao, Y. Jiang, M. Zhao, X. Liu, and J. Li, "Computer virtual experiment on fluidized beds using a coarse-grained discrete particle method-EMMS-DPM," Chem. Eng. Sci. **155**, 314–337 (2016).
[36]C. K. K. Lun, S. B. Savage, D. J. Jeffrey, and N. Chepurniy, "Kinetic theories for granular flow: Inelastic particles in Couette flow and slightly inelastic particles in a general flowfield," J. Fluid Mech. **140**, 223–256 (1984).
[37]D. L. Marchisio and R. O. Fox, *Computational Models for Polydisperse Particulate and Multiphase Systems* (Cambridge University Press, 2013).
[38]B. Meng, J. Zeng, B. Tian, L. Li, Z. He, and X. Guo, "Modeling and verification of the Richtmyer–Meshkov instability linear growth rate of the dense gas-particle flow," Phys. Fluids **31**(7), 074102 (2019).
[39]J. J. Nieuwland, M. L. Veenendaal, J. A. M. Kuipers, and W. P. M. Van Swaaij, "Bubble formation at a single orifice in gas-fluidised beds," Chem. Eng. Sci. **51**(17), 4087–4102 (1996).
[40]P. J. O'Rourke and D. M. Snider, "Inclusion of collisional return-to-isotropy in the MP-PIC method," Chem. Eng. Sci. **80**, 39–54 (2012).
[41]P. J. O'Rourke, P. Pinghua Zhao, and D. Snider, "A model for collisional exchange in gas/liquid/solid fluidized beds," Chem. Eng. Sci. **64**(8), 1784–1797 (2009).
[42]A. Panchal and S. Menon, "A hybrid Eulerian-Eulerian/Eulerian-Lagrangian method for dense-to-dilute dispersed phase flows," J. Comput. Phys. **439**, 110339 (2021).
[43]A. Passalacqua, R. O. Fox, R. Garg, and S. Subramaniam, "A fully coupled quadrature-based moment method for dilute to moderately dilute fluid–particle flows," Chem. Eng. Sci. **65**(7), 2267–2283 (2010).
[44]X. Pialat, O. Simonin, and P. Villedieu, "A hybrid Eulerian-Lagrangian method to simulate the dispersed phase in turbulent gas-particle flows," Int. J. Multiphase Flow **33**(7), 766–788 (2007).
[45]D. Queteschiner, T. Lichtenegger, S. Schneiderbauer, and S. Pirker, "Coupling resolved and coarse-grain DEM models," Part. Sci. Technol. **36**(4), 517–522 (2018).
[46]S. M. Rao, K. Zhu, C.-H. Wang, and S. Sundaresan, "Electrical capacitance tomography measurements on the pneumatic conveying of solids," Ind. Eng. Chem. Res. **40**(20), 4216–4226 (2001).
[47]S. Rauchenzauner and S. Schneiderbauer, "A dynamic spatially averaged two-fluid model for heat transport in moderately dense gas–particle flows," Phys. Fluids **32**(6), 063307 (2020).
[48]M. Sakai and S. Koshizuka, "Large-scale discrete element modeling in pneumatic conveying," Chem. Eng. Sci. **64**(3), 533–539 (2009).
[49]R. Saurel and R. Abgrall, "A multiphase Godunov method for compressible multifluid and multiphase flows," J. Comput. Phys. **150**(2), 425–467 (1999).
[50]R. Saurel, A. Chinnayya, and Q. Carmouze, "Modelling compressible dense and dilute two-phase flows," Phys. Fluids **29**(6), 063301 (2017).
[51]S. Schneiderbauer, A. Aigner, and S. Pirker, "A comprehensive frictional-kinetic model for gas–particle flows: Analysis of fluidized and moving bed regimes," Chem. Eng. Sci. **80**, 279–292 (2012).
[52]J. C. Schulz, K. C. Gottiparthi, and S. Menon, "Richtmyer-Meshkov instability in dilute gas-particle mixtures with re-shock," Phys. Fluids **25**(11), 114105 (2013).
[53]K. Shimura and A. Matsuo, "Two-dimensional CFD–DEM simulation of vertical shock wave-induced dust lifting processes," Shock Waves **28**(6), 1285–1297 (2018).
[54]A. Srivastava and S. Sundaresan, "Analysis of a frictional-kinetic model for gas-particle flow," Powder Technol. **129**(1–3), 72–85 (2003).
[55]W. Sun, S. Jiang, and K. Xu, "An asymptotic preserving unified gas kinetic scheme for gray radiative transfer equations," J. Comput. Phys. **285**, 265–279 (2015).
[56]S. Tan, W. Sun, K. Xu, J. Wei, and G. Ni, "Time implicit unified gas kinetic scheme for 3D multi-group neutron transport simulation," Commun. Comput. Phys. **28**(3), 1189–1218 (2020).
[57]S. Tao, H. Zhang, Z. Guo, and L.-P. Wang, "A combined immersed boundary and discrete unified gas kinetic scheme for particle–fluid flows," J. Comput. Phys. **375**, 498–518 (2018).
[58]E. F. Toro, *Riemann Solvers and Numerical Methods for Fluid Dynamics: A Practical Introduction* (Springer Science and Business Media, 2013).
[59]Y. Tsuji, "Multi-scale modeling of dense phase gas–particle flow," Chem. Eng. Sci. **62**(13), 3410–3418 (2007).
[60]Y. Tsuji, T. Kawaguchi, and T. Tanaka, "Discrete particle simulation of two-dimensional fluidized bed," Powder Technol. **77**(1), 79–87 (1993).
[61]M. A. van der Hoef, M. van Sint Annaland, N. G. Deen, and J. A. M. Kuipers, "Numerical simulation of dense gas-solid fluidized beds: A multiscale modeling strategy," Annu. Rev. Fluid Mech. **40**(1), 47–70 (2008).
[62]M. A. van der Hoef, M. Ye, M. van Sint Annaland, A. T. Andrews, S. Sundaresan, and J. A. M. Kuipers, "Multiscale modeling of gas-fluidized beds," Adv. Chem. Eng. **31**, 65–149 (2006).
[63]J. Wang, "Continuum theory for dense gas-solid flow: A state-of-the-art review," Chem. Eng. Sci. **215**, 115428 (2020).
[64]Z. Wang and H. Yan, "Unified gas-kinetic particle method for dilute granular flow and its application in a solid jet," Acta Mech. Sin. **36**(1), 22–34 (2020).
[65]K. Xu, "Gas-kinetic schemes for unsteady compressible flow simulations," in *Proceedings of the 29th Computational Fluid Dynamics*, Lecture Series—von Karman Institute for Fluid Dynamics (van Karman Institute, 1998), Vol. 3, pp. C1–C202.
[66]K. Xu, "A gas-kinetic BGK scheme for the Navier–Stokes equations and its connection with artificial dissipation and Godunov method," J. Comput. Phys. **171**(1), 289–335 (2001).
[67]K. Xu, *Direct Modeling for Computational Fluid Dynamics: Construction and Application of Unified Gas-Kinetic Schemes* (World Scientific, 2014), Vol. 4.
[68]K. Xu, *A Unified Computational Fluid Dynamics Framework from Rarefied to Continuum Regimes*, Elements in Aerospace Engineering (Cambridge University Press, 2021).
[69]K. Xu and J.-C. Huang, "A unified gas-kinetic scheme for continuum and rarefied flows," J. Comput. Phys. **229**(20), 7747–7764 (2010).
[70]X. Xu, Y. Chen, and K. Xu, "Modeling and computation for non-equilibrium gas dynamics: Beyond single relaxation time kinetic models," Phys. Fluids **33**(1), 011703 (2021).

[71]X. Yang, X. Ji, W. Shyy, and K. Xu, "Comparison of the performance of high-order schemes based on the gas-kinetic and HLLC fluxes," J. Comput. Phys. **448**, 110706 (2022).
[72]X. Yang, C. Liu, X. Ji, W. Shyy, and K. Xu, "Unified gas-kinetic wave-particle methods. VI. Disperse dilute gas-particle multiphase flow," arXiv:2107.05075 (2021).
[73]Q. Zhang, W. Cai, C. Lu, D. Gidaspow, and H. Lu, "Modified MFIX code to simulate hydrodynamics of gas-solids bubbling fluidized beds: A model of coupled kinetic theory of granular flow and discrete element method," Powder Technol. **357**, 417–427 (2019).
[74]Y. Zhang, X.-B. Lu, and X.-H. Zhang, "An optimized Eulerian–Lagrangian method for two-phase flow with coarse particles: Implementation in open-source field operation and manipulation, verification, and validation," Phys. Fluids **33**(11), 113307 (2021).
[75]F. Zhao, X. Ji, W. Shyy, and K. Xu, "Compact higher-order gas-kinetic schemes with spectral-like resolution for compressible flow simulations," Adv. Aerodyn. **1**(1), 13 (2019).
[76]W. Zhong, A. Yu, G. Zhou, J. Xie, and H. Zhang, "CFD simulation of dense particulate reaction system: Approaches, recent advances and applications," Chem. Eng. Sci. **140**, 16–43 (2016).
[77]Y. Zhu, C. Liu, C. Zhong, and K. Xu, "Unified gas-kinetic wave-particle methods. II. Multiscale simulation on unstructured mesh," Phys. Fluids **31**(6), 067105 (2019).